J. Fluid Mech. (2013), *vol.* 717, *pp.* 417–448.
doi:10.1017/jfm.2012.585

Convectons in a rotating fluid layer

Cédric Beaume[1,†], Alain Bergeon[1], Hsien-Ching Kao[2] and Edgar Knobloch[2]

[1]INPT, UPS, IMFT (Institut de Mécanique des Fluides de Toulouse), Université de Toulouse, Allée Camille Soula, F-31400 Toulouse, France and CNRS, IMFT, F-31400 Toulouse, France
[2]Department of Physics, University of California, Berkeley, CA 94720, USA

(Received 27 April 2012; revised 10 September 2012; accepted 23 November 2012)

Two-dimensional convection in a plane layer bounded by stress-free perfectly conducting horizontal boundaries and rotating uniformly about the vertical is considered. Time-independent spatially localized structures, called convectons, of even and odd parity are computed. The convectons are embedded within a self-generated shear layer with a compensating shear flow outside the structure. These states are organized within a bifurcation structure called slanted snaking and may be present even when periodic convection sets in supercritically. These interesting properties are traced to the presence of a conserved quantity and hence to the use of stress-free boundary conditions.

Key words: nonlinear dynamical systems, pattern formation, rotating flows

1. Introduction

Convection in a horizontal fluid layer rotating about the vertical provides one of the classical examples of hydrodynamic instability (Veronis 1959; Chandrasekhar 1961). The system is of interest because convection can set in either via an exchange of stability (a steady-state bifurcation) or via overstability (a Hopf bifurcation) depending on the Prandtl and Taylor numbers (Veronis 1959; Chandrasekhar 1961; Clune & Knobloch 1993; Bajaj, Ahlers & Pesch 2002). In the weakly nonlinear regime classical perturbation theory has revealed branches of steady convection (both two- and three-dimensional (Veronis 1959; Goldstein, Knobloch & Silber 1990, 1992)) near the steady-state bifurcation and branches of different types of standing and travelling waves near the Hopf bifurcation (Veronis 1959; Silber & Knobloch 1990, 1993), as reviewed elsewhere (Knobloch 1998). When these bifurcations are near one another (i.e. the rotation rate as measured by the dimensionless Taylor number is near a special value called a codimension-two point) one can study the interaction between steady and oscillatory convection at small amplitude. This study has revealed different ways whereby oscillations, be they in the form of standing or travelling waves, give way to steady convection as the Rayleigh number increases (Guckenheimer & Knobloch 1983).

In this paper we examine this classical problem from a new point of view and study steady but spatially *localized* structures. Following Blanchflower (1999) we refer to

† Email address for correspondence: ced.beaume@gmail.com

such states as *convectons*. For this purpose we adopt the two-dimensional formulation and suppose that the horizontal extent of the layer is sufficiently small that the Froude number remains small (i.e. the centrifugal force may be neglected) while at the same time being sufficiently large that well-localized structures are permitted.

Classical theory of localized states as exemplified by the Swift–Hohenberg equation (Burke & Knobloch 2007) shows that steady, spatially localized states are found in the region of bistability between the conduction state and spatially periodic convection. These states are organized in the so-called snakes-and-ladders structure consisting of a pair of intertwined branches of states of even and odd parity linked by rung-like branches consisting of asymmetric states. As one follows the branches to larger energy the localized states add cells on either side, maintaining symmetry, and so grow in length until the domain is filled with convection. This type of behaviour has now been seen in a large variety of fluid flows (Batiste *et al.* 2006; Assemat, Bergeon & Knobloch 2008; Bergeon & Knobloch 2008; Lo Jacono, Bergeon & Knobloch 2010; Schneider, Gibson & Burke 2010; Beaume, Bergeon & Knobloch 2011).

However, with stress-free velocity boundary conditions the equations describing two-dimensional rotating convection conserve the integral of the transverse or *zonal* velocity and this special property of the equations allows localized states to be present outside of the region of bistability and indeed when spatially periodic convection sets in supercritically and no bistability is present at all. In this paper we provide numerical evidence backing these conclusions and relate them to the presence of the conserved quantity and the associated modulational instability (Cox & Matthews 2001).

This paper is organized as follows. In § 2 we introduce the formulation of the problem. In § 3 we compute spatially localized states and show that they exhibit *slanted* snaking. In § 4 we use the amplitude equation approach to study the bifurcation to convectons. In § 5 we use multiscale perturbation theory to explain various aspects of the numerical results. Brief conclusions follow in § 6.

2. Governing equations

The dimensionless equations governing two-dimensional convection in a Boussinesq layer rotating uniformly about the vertical with angular velocity Ω take the form

$$Ra\theta_x - Tv_z + \nabla^4\psi = \sigma^{-1}[\nabla^2\psi_t + J(\psi, \nabla^2\psi)], \tag{2.1}$$

$$\psi_x + \nabla^2\theta = \theta_t + J(\psi, \theta), \tag{2.2}$$

$$T\psi_z + \nabla^2 v = \sigma^{-1}[v_t + J(\psi, v)]. \tag{2.3}$$

Here $\boldsymbol{u} \equiv (-\psi_z, v, \psi_x)$ is the velocity in the rotating frame with (x, y, z) as coordinates and $\psi(x, z, t)$ is the poloidal streamfunction. The quantity $v(x, z, t)$ represents the zonal velocity while θ represents the departure of the temperature Θ from the conduction profile, and $J(\psi, \cdot) \equiv \psi_x(\cdot)_z - (\cdot)_x\psi_z$. To write these equations, we used the height h of the layer as the unit of length, the thermal diffusion time h^2/κ, where κ is the thermal diffusivity, as the unit of time and the imposed temperature difference $\Delta\Theta$ as the unit of temperature. The resulting system is specified by the following dimensionless numbers: the Prandtl number σ, the Rayleigh number Ra and the Taylor number T defined by

$$\sigma = \frac{\nu}{\kappa}, \quad Ra = \frac{g\alpha\Delta\Theta h^3}{\kappa\nu}, \quad T = \frac{2\Omega h^2}{\nu}. \tag{2.4}$$

Here ν is the kinematic viscosity, g is the gravitational acceleration and α is the thermal expansion coefficient in the Boussinesq approximation. As defined T is the inverse Ekman number; in other papers the term Taylor number is used to refer to T^2.

We impose stress-free and fixed-temperature boundary conditions at the top and bottom

$$\psi = \psi_{zz} = \theta = v_z = 0 \quad \text{at } z \in \{0, 1\} \tag{2.5}$$

with periodic boundary conditions (PBC) in the horizontal with period Γ that is large compared with the onset wavelength λ_c of convection. With these boundary conditions, the system possesses the trivial solution $\psi = \theta = v = 0$, corresponding to the conduction state. This solution is present for all values of the Rayleigh number Ra and its instability as Ra increases is responsible for the presence of convection as described by Veronis (1959). The properties of the convecting state that results are in turn affected by the symmetries of (2.1)–(2.3) with the boundary conditions (2.5). These include equivariance under horizontal translations, $x \to x + \ell$, $(\psi, \theta, v) \to (\psi, \theta, v)$, as well as the following two reflections:

$$R_1: \quad (x, z) \to (-x, z), \quad (\psi, \theta, v) \to (-\psi, \theta, -v), \tag{2.6a}$$

$$R_2: \quad (x, z) \to (x, 1 - z), \quad (\psi, \theta, v) \to (-\psi, -\theta, v). \tag{2.6b}$$

Non-trivial solutions invariant under R_1 have even parity under reflection in $x = 0$ while those invariant under the point symmetry $R_1 \circ R_2$ have odd parity in the midplane $z = 1/2$. In the following we refer to localized states with these properties as L^+ and L^-, respectively. R_2-symmetric solutions are only present at much larger Rayleigh numbers and will not be considered in this paper.

The stress-free boundary conditions (2.5) play an important role in what follows since with these boundary conditions v is defined only up to a constant, i.e. v is a phase-like variable. Moreover

$$\frac{\mathrm{d}}{\mathrm{d}t}\bar{V} = 0, \quad \bar{V} \equiv \int_D v(x, z, t)\, \mathrm{d}x\, \mathrm{d}z, \tag{2.7}$$

where D refers to the domain $[-\Gamma/2, \Gamma/2] \times [0, 1]$, implying that $\bar{V}$ remains constant during time evolution. A similar situation arises in convection in a vertical magnetic field where the magnetic vector potential is phase-like and the conserved quantity is the vertical magnetic flux, as emphasized by Cox & Matthews (2001).

In the following, we compute stationary solutions of the equations using a numerical continuation algorithm based on a Newton solver. The implementation of the method follows that of Mamun & Tuckerman (1995) but uses a spectral element discretization in the horizontal. In each element, the fields are approximated by a high-order interpolant through the Gauss–Lobatto–Legendre points. The Newton solver requires a first-order time integration scheme for the equations; we use a scheme in which the diffusive linear part of the equations is treated implicitly and the nonlinear part explicitly. Each time step therefore requires the inversion of four Helmholtz problems. These are inverted by combining a Schur decomposition on the elements and diagonalization in z. We take full advantage of the symmetries of the equations to compute different spatially localized solutions. The computations employ approximately two spectral elements per critical wavelength λ_c, each element being meshed by a 15×11 Gauss–Lobatto–Legendre grid. Calculations with this resolution are well converged even at the highest Rayleigh numbers employed. The continuation algorithm has been used to study other systems where convectons are present, including magnetoconvection (Lo Jacono, Bergeon & Knobloch 2011).

3. Results

In this section, we discuss time-independent solutions of (2.1)–(2.3) with the boundary conditions (2.5) and PBC in the horizontal, focusing on spatially localized states. We first consider the so-called subcritical regime and demonstrate the presence of slanted snaking in this regime. We then proceed to the supercritical regime and reveal that very similar behaviour occurs in this regime as well. In both cases we discuss the role played by the Taylor number. Our solutions are computed with $\bar{V} = 0$ implicitly enforced by imposing the symmetry R_1 or $R_1 \circ R_2$. Each choice results in a distinct branch of localized solutions.

3.1. *Localized states in the subcritical regime*

As Ra increases steady convection sets in at Ra_c independently of the value of the Prandtl number σ. As the Taylor number increases Ra_c moves to higher values: rotation stabilizes the conduction state against convection. For small Taylor numbers convection is supercritical but becomes subcritical with increasing Taylor number whenever the Prandtl number is sufficiently small. This is so for both stress-free and no-slip boundary conditions (Goldstein *et al.* 1990; Clune & Knobloch 1993). For yet larger rotation rates the steady onset is preceded by a Hopf bifurcation. In contrast, when $\sigma > 0.676605$ the onset is steady regardless of the Taylor number and convection is always supercritical (Goldstein *et al.* 1990).

In this section we describe the results for $\sigma = 0.1$ and several different values of T. Figure 1 shows the average poloidal kinetic energy,

$$\mathscr{E} \equiv \frac{1}{2\Gamma} \int_D (\psi_x^2 + \psi_z^2)\, \mathrm{d}x\, \mathrm{d}z, \tag{3.1}$$

as a function of the Rayleigh number Ra when $T = 20$. For this value of T convection sets in at $Ra_c \approx 1179.2$ and it does so with critical wavenumber $k_c \approx 3.1554$. The results are obtained in a periodic domain of length $\Gamma = 10\lambda_c$, where the critical wavelength $\lambda_c \equiv 2\pi/k_c$ depends on the Taylor number and decreases as T increases. The figure shows the branch of steady periodic convection with 10 wavelengths in the domain, labelled P_{10}. The branch bifurcates strongly subcritically but turns around at a saddle-node at $Ra \approx 913$. The figure also shows a pair of branches of even and odd parity localized states, labelled $L_{10}^{\pm}$, that bifurcate from P_{10} at small amplitude ($Ra \approx 1175$, $\mathscr{E} \approx 0.004$, see figure 4). These branches also bifurcate subcritically. Initially both solutions take the form of weakly modulated wavetrains, but as Ra approaches the leftmost saddle-nodes at $Ra \approx 807$ the modulation becomes strongly nonlinear resulting in the formation of well-localized convectons of even and odd parity (figure 2). Beyond the leftmost saddle-nodes the two branches intertwine forming a structure that has been called *slanted snaking* (Firth, Columbo & Scroggie 2007; Dawes 2008). As one follows the two branches in the direction of increasing energy the convectons gradually increase in length by nucleating new cells at either end. Because of the slant in the snaking structure the localized states move towards larger values of the Rayleigh number and their wavelength grows (figure 2). As a result of this Rayleigh number dependence of the convecton wavelength the domain Γ becomes almost full when the convectons have grown to 4 wavelengths. At this point the structure resembles a periodic wavetrain with defects a distance Γ apart and the snaking stops. The branches now undergo a loop required to squeeze in an extra pair of cells and terminate on P_5 with 5 wavelengths in the domain Γ (figure 1).

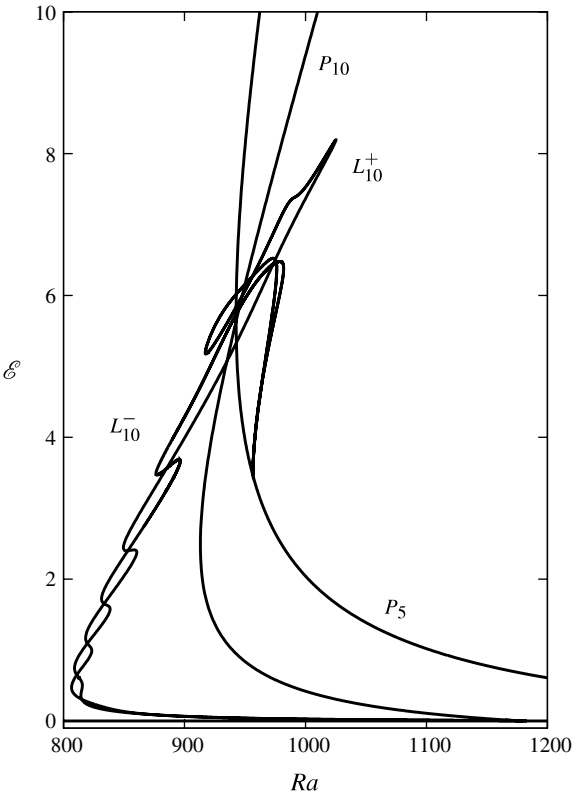

FIGURE 1. Bifurcation diagram showing the average poloidal kinetic energy $\mathscr{E}$ as a function of the Rayleigh number Ra for slanted snaking when $T = 20$ and $\sigma = 0.1$. The branches of localized states $L_{10}^{\pm}$ in a $\Gamma = 10\lambda_c$ domain are shown. They bifurcate in a secondary bifurcation on the branch P_{10} of periodic convection with 10 pairs of counter-rotating rolls in Γ and connect to P_5, the branch of 5 pairs of counter-rotating rolls in Γ. The solutions at each saddle-node during the snaking process are shown in figure 2.

The lower panels figure 2 show the profile of the depth-integrated zonal velocity

$$V(x) \equiv \int_0^1 v(x, z)\, \mathrm{d}z. \tag{3.2}$$

We see that the presence of convection imprints a step-like structure on this profile much as occurs in the corresponding magnetoconvection problem with imposed vertical magnetic field (Lo Jacono *et al.* 2011). This structure turns into a saw-tooth profile by the time the branches terminate on the branch P_5 of periodic states. To understand this behaviour we first note that the symmetry R_2 implies that clockwise and counterclockwise cells have the same effect on $V(x)$; moreover, the symmetry R_1 implies that the slope of $V(x)$ is unaffected by reflection in $x = 0$. In the periodic state (top solutions) $V(x)$ varies linearly across each convection cell with steeper diffusive layers of the opposite slope between adjacent cells. These diffusive layers are quite broad since their dimensional width is $Re^{-1/2}h$, where $Re \equiv Uh/\nu$ is the Reynolds number; since the flow speed $U \sim \kappa/h$ when $Ra \sim Ra_c$ the dimensionless width $\sim\sigma^{1/2}$.

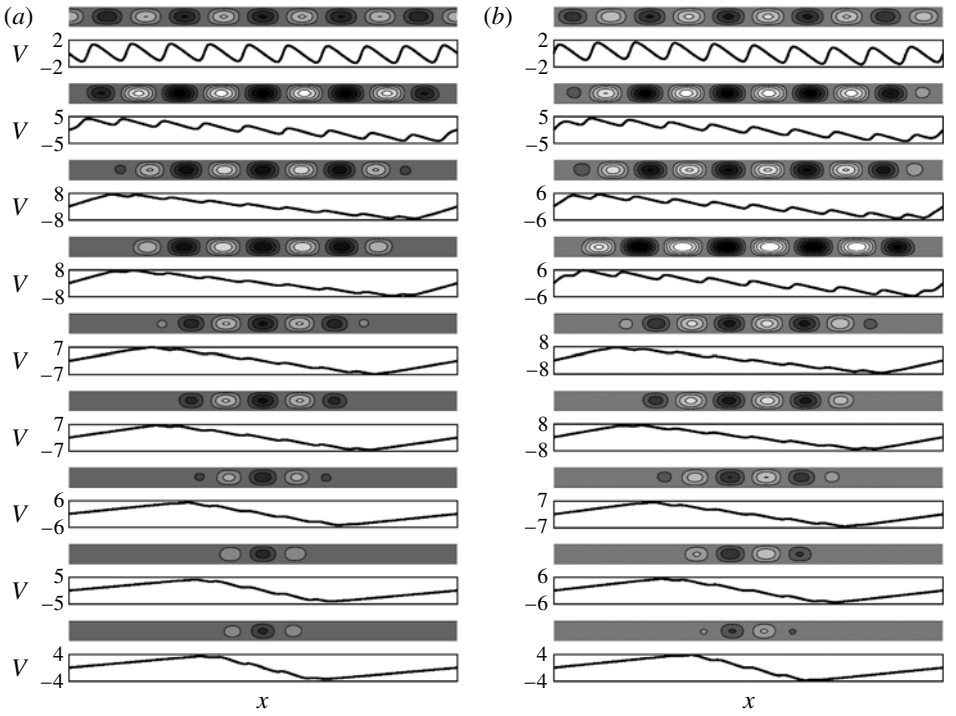

FIGURE 2. Solution profiles at successive saddle-nodes on (*a*) L_{10}^{-} and (*b*) L_{10}^{+} in figure 1. Upper panels show isovalues of the streamfunction with light (dark) regions corresponding to clockwise (counterclockwise) flow. Lower panels show the profiles of $V(x)$. Topmost solutions correspond to the termination point on P_5.

The effect of the cellular motion outside these layers is most easily discussed in terms of the relation

$$\sigma \frac{\mathrm{d}V}{\mathrm{d}x} = -\int_0^1 \psi_z v \, \mathrm{d}z, \tag{3.3}$$

obtained from (2.3) upon integration over z followed by integration once in x. Thus non-zero values of the averaged Reynolds stress are responsible for the presence of a linear profile $V(x)$ across the cell.

These ideas extend to the whole convecton itself. Figure 2 shows that each convecton is accompanied, regardless of parity, by a non-zero shear across it. This shear can be quantified by

$$\Delta V \equiv V(x = L/2) - V(x = -L/2), \tag{3.4}$$

where L is the length of the convecton. The average shear generated by the presence of the convecton is therefore $\Delta V/L$ with the cellular structure imprinted on this background shear. Of course in view of PBC the shear generated by the convecton must be compensated by equal and opposite shear in the convection-free part of the domain. The presence of this compensating shear is also seen in figure 2.

In the following we define the convecton length L as the distance between the global maxima and minima of the zonal velocity $V(x)$ and show in figure 3(*a*) the corresponding velocity difference $|\Delta V|$ for the solutions shown in figure 2 and in

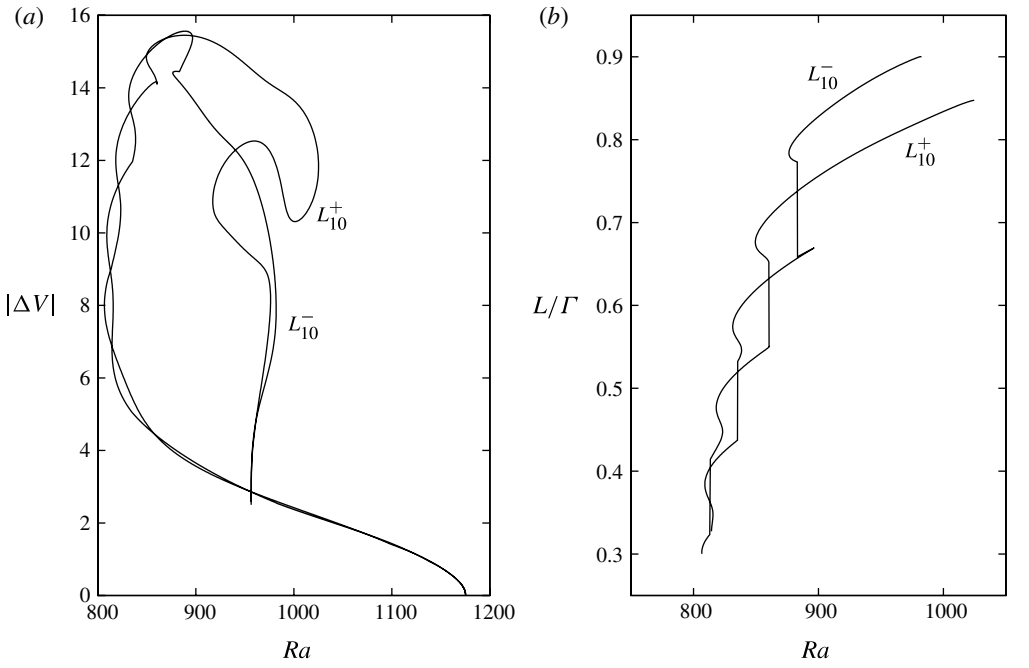

FIGURE 3. Properties of the convectons computed in figure 1. (*a*) Jump $|\Delta V|$ in zonal velocity across the convecton and (*b*) convecton length L relative to the domain period $\Gamma = 10\lambda_c$, both as functions of the Rayleigh number Ra. The length L is shown for the slanted snaking branch between the leftmost and rightmost saddle-nodes only since its determination requires that the convectons be well localized. Discontinuities (vertical jumps) correspond to nucleation of new cells.

figure 3(*b*) the fraction L/Γ of the domain Γ occupied by the convecton, both as functions of Ra. Both even- and odd-parity convectons have similar lengths L at corresponding Rayleigh numbers and generate similar values of ΔV. The resulting shear rate $V'(x) \sim \Delta V/L$ reduces the local rotation rate quite substantially. For example, when $T = 20$ and $\sigma = 0.1$ the maximum value of the quantity $|\Delta V|/\sigma LT \approx 0.7$ occurs at $Ra \approx 810$ and represents a 70 % reduction in the local rotation rate.

3.2. *Effect of domain size*

Figure 4 shows the effect of varying the domain size Γ and compares the bifurcation diagrams for $\Gamma = 10\lambda_c$, $15\lambda_c$ and $20\lambda_c$, all for $T = 20$ and $\sigma = 0.1$. As Γ increases the secondary bifurcation on P_{10} that creates the localized states moves to smaller and smaller amplitude (figure 4*a*) while the leftmost saddle-nodes on $L^{\pm}$ shift towards lower Rayleigh numbers ($Ra \approx 807$ for $L_{10}^{\pm}$, $Ra \approx 798$ for $L_{15}^{\pm}$, $Ra \approx 793$ for $L_{20}^{\pm}$, $Ra \approx 787$ for $L_{40}^{\pm}$). Moreover, beyond the leftmost saddle-node $\mathscr{E}$ increases with Ra at the same rate in all cases. At the same time the number of saddle-nodes on each branch increases in proportion to Γ. A careful examination of the solution profiles in each case indicates that the nucleation of new cells can be associated with the saddle-nodes on the left, with the new cells at full strength by the time one reaches the next saddle-node on the right. Thus in larger domains new cells are nucleated faster in such a way that at a fixed value of Ra the convectons fill the same fraction

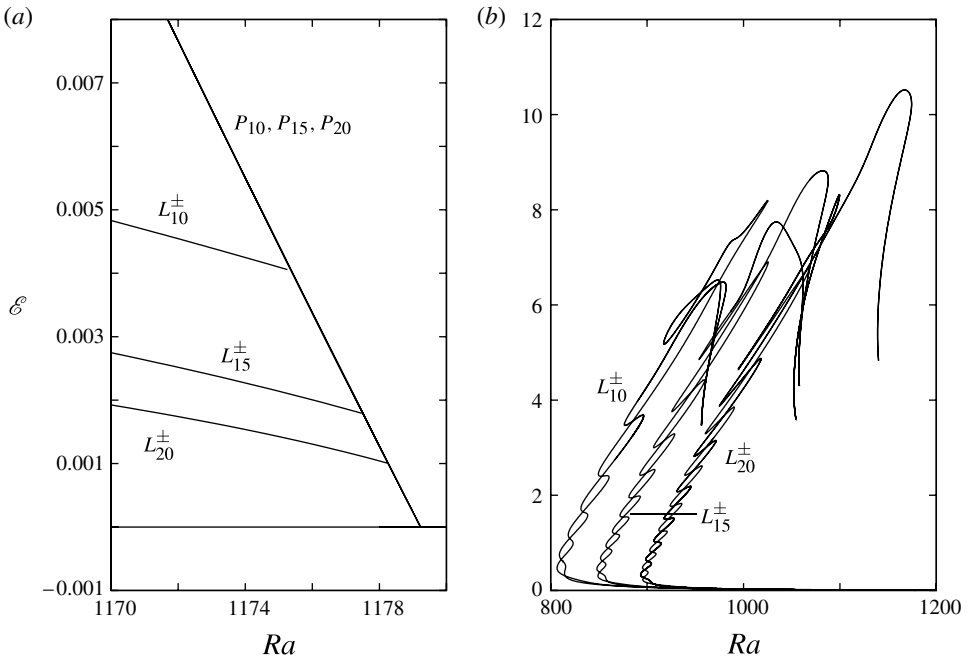

FIGURE 4. Bifurcation diagram showing the average poloidal kinetic energy $\mathscr{E}$ as a function of the Rayleigh number Ra for various domain sizes Γ at $T = 20$ and $\sigma = 0.1$. (*a*) Small-amplitude behaviour: the branches P_n of periodic convection coincide, but the convecton branches $L_n^{\pm}$ move to lower amplitude as Γ increases. At these values of Ra the $L_n^{\pm}$ branches are exponentially close for each n and hence indistinguishable. (*b*) Comparison between branches of localized states for $\Gamma = 10\lambda_c$, $15\lambda_c$ and $20\lambda_c$. For clarity, the branches for $\Gamma = 15\lambda_c$ and $\Gamma = 20\lambda_c$ have been displaced to $Ra + 50$ and $Ra + 100$, respectively, i.e. in proportion to Γ.

of the available domain. Figure 4(*b*) also reveals that the saddle-nodes occur more frequently for smaller values of Ra than for larger Ra. This is a consequence of the wavelength change that occurs with increasing Ra: because of this wavelength change the structure expands with Ra and so fewer nucleation events become necessary to maintain the growth rate of the structure with increasing Ra. Figure 4(*b*) suggests that this growth rate is constant in Ra and Γ-independent. Computation of the wavelength within the localized structure as a function of Ra shows that the $L_{20}^{\pm}$ branches bifurcate from P_{20} with wavelength $\lambda \approx 1.9912$; L_{20}^{+} terminates on P_{10} with $\lambda \approx 3.9825$ while L_{20}^{-} terminates on P_9 with $\lambda \approx 4.4250$. Most of the required wavelength increase occurs along the lower convecton branch, prior to the leftmost saddle-node, growing from $\lambda \approx 1.9912$ at the initial bifurcation point to $\lambda \simeq 3.6$ at the leftmost saddle-node. Beyond the saddle-node, within the interval of slanted snaking, the wavelength varies linearly with Ra but the cumulative increase in the wavelength is less than on the lower branch.

Figure 5(*a*) shows the *total* poloidal kinetic energy $E \equiv (1/2)\int_D (\psi_x^2 + \psi_z^2)\,\mathrm{d}x\,\mathrm{d}z$ as a function of Ra for $\Gamma = 20\lambda_c$ and $\Gamma = 40\lambda_c$. This representation separates the two branches and demonstrates the presence of the extra saddle-nodes required for the localized structure to grow at twice the rate for $\Gamma = 40\lambda_c$ as for $\Gamma = 20\lambda_c$. In particular, the figure employs vertical lines to indicate the correspondence between

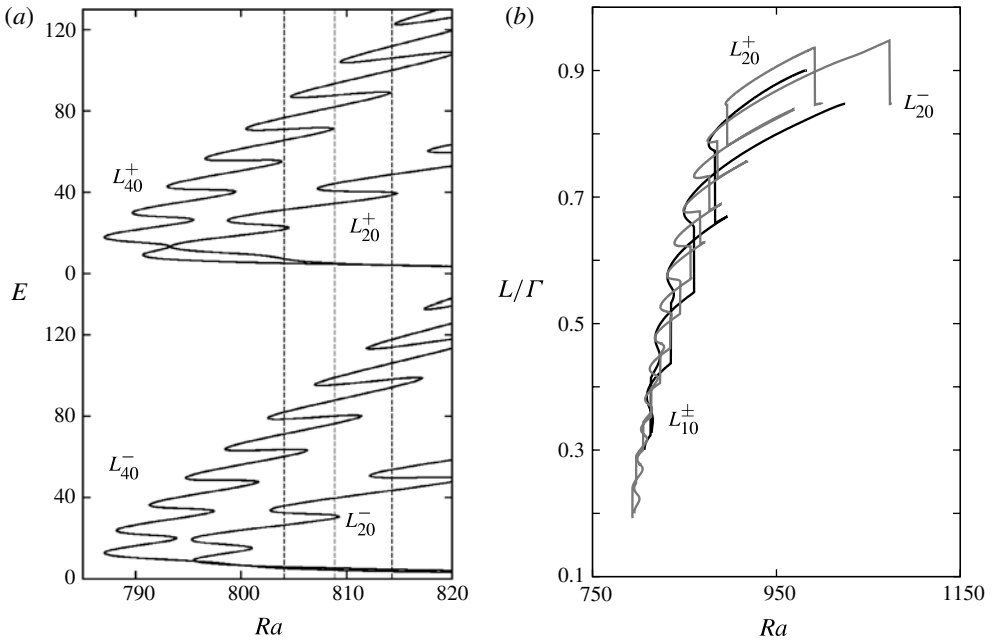

FIGURE 5. (*a*) The total poloidal kinetic energy E for $L_{20}^{\pm}$ ($\Gamma = 20\lambda_c$) and $L_{40}^{\pm}$ ($\Gamma = 40\lambda_c$) as a function of the Rayleigh number Ra. The vertical dashed lines indicate the alignment of the saddle-nodes. Upper curves: even-parity convectons. Lower curves: odd-parity convectons. (*b*) The fraction of the domain period Γ occupied by both even- and odd-parity convectons when $\Gamma = 10\lambda_c$ (black lines) and $\Gamma = 20\lambda_c$ (grey lines).

the right saddle-nodes along the L_{20}^{+} and L_{40}^{+} branches and reveals that every second right saddle-node on L_{40}^{+} aligns with the corresponding right saddle-node on L_{20}^{+}. The intervening right saddle-nodes on L_{40}^{+} align with those of L_{20}^{-}, since L_{40}^{+} possesses twice the number of cells as $L_{20}^{\pm}$ at the same Rayleigh number, so the 8-roll saddle-node solution on L_{40}^{+} aligns with the 4-roll saddle-node solution on L_{20}^{+} while the 10-roll saddle-node solution on L_{40}^{+} aligns with the 5-roll saddle-node solution on L_{20}^{-} and so on. Figure 5(*b*) confirms the conclusion that convectons grow in length at twice the rate when the domain size is doubled by showing the fraction of the domain period occupied by even- and odd-parity convectons when $\Gamma = 10\lambda_c$ and when $\Gamma = 20\lambda_c$.

3.3. *Effect of rotation rate*

When rotation is absent the problem reduces to Rayleigh–Bénard convection which is supercritical and free from localized structures. In figure 6 we show how this picture changes as the Taylor number increases. Each panel in the figure is computed for the same Prandtl number $\sigma = 0.1$ and $\Gamma = 10\lambda_c$ as used for figure 1 for $T = 20$. Since the critical wavelength λ_c decreases with increasing T this choice implies that the aspect ratio used also decreases with T. Since motion relieves the stabilizing constraints of rotation convection quickly becomes subcritical as T increases. Figure 6 shows that this is already so for $T = 10$ and reveals that at this rotation rate the leftmost saddle-nodes of both the periodic states and the localized states are close together. Since the latter lies below the saddle-node of the periodic state some localized states already fall outside the region of bistability between the periodic and conduction states. As T increases both saddle-nodes move towards larger Ra but the saddle-node of the

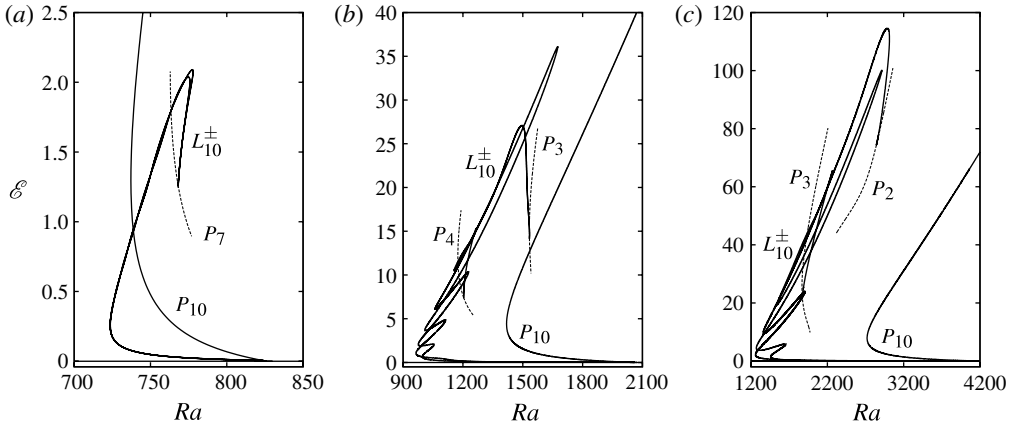

FIGURE 6. Bifurcation diagrams $\mathscr{E}(Ra)$ displaying the branches $L_{10}^{\pm}$ of localized states together with the P_{10} branch from which they bifurcate, all for $\sigma = 0.1$ and $\Gamma = 10\lambda_c$. The periodic branch(es) on which the $L_{10}^{\pm}$ terminate is (are) not shown in their entirety (see table 1). (*a*) $T = 10$; (*b*) $T = 40$; and (*c*) $T = 80$. Figure 1 shows the case $T = 20$.

T	10	20	40	80
λ_c	2.423	1.991	1.552	1.198
Ra_c	826	1179	2068	4195
Left saddle-node of P_{10}	737	913	1418	2721
Left edge of snaking	723	806	964	1258
Right edge of snaking	778	1025	1675	3013
Connects to	P_7	P_5	P_4 (L_{10}^-) and P_3 (L_{10}^+)	P_3 (L_{10}^-) and P_2 (L_{10}^+)
with wavelength	3.64	3.98	3.88 (L_{10}^-) and 5.17 (L_{10}^+)	3.99 (L_{10}^-) and 5.99 (L_{10}^+)

TABLE 1. Characteristics of slanted snaking for $\sigma = 0.1$, $\Gamma = 10\lambda_c$ and different values of T.

periodic states does so much faster, thereby opening an increasingly wide Rayleigh number interval in which localized states fall outside the bistability region. This is a consequence of the higher rotation rate which stabilizes the conduction state and pushes Ra_c higher. This stabilizing effect is present at finite amplitude as well but is reduced for the localized states from that prevailing for the periodic states by the shear $\Delta V/L$ that accompanies their presence. As a result the full Rayleigh number interval in which localized states are present also grows rapidly with the rotation rate (figure 6 and table 1). The right edge of this interval is determined by the rightmost saddle-node but in all cases studied this point is not far from the saddle-node on the branch of periodic states on which the convectons terminate. This is a consequence of the strong Rayleigh number dependence of the wavelength within the convectons which prevents their termination until periodic states of the right wavelength are present. Of course, in cases in which the convecton wavelength is strongly incommensurate with the domain period the wavelength at termination may differ substantially from the preferred wavelength, as discussed in detail by Bergeon *et al.* (2008). This is the case, for example, for $T = 40$ and $T = 80$ in figure 6(*b*,*c*) for which the $L_{10}^{\pm}$ branches terminate on different periodic branches (see table 1).

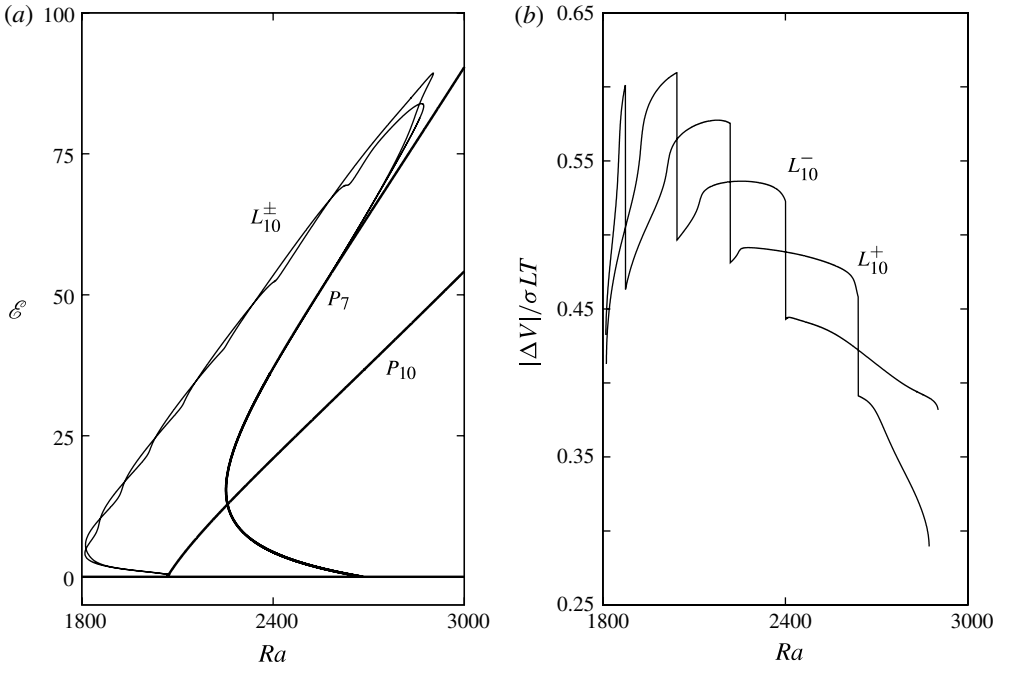

FIGURE 7. (*a*) Bifurcation diagram showing the average poloidal kinetic energy $\mathscr{E}$ as a function of the Rayleigh number Ra for the periodic states P_{10}, P_7 and for the branches $L_{10}^{\pm}$ of spatially localized states. (*b*) The local reduction in the rotation rate within the localized structures as measured by the quantity $|\Delta V|/\sigma LT$ between the leftmost and rightmost saddle-nodes on both slanted snaking branches, where L is the convecton length. The parameters are $T = 40$, $\sigma = 0.6$ and $\Gamma = 10\lambda_c$.

Figure 6 also reveals that as T decreases from larger values the amplitude of the oscillations of $L^{\pm}$ about the overall slope gradually decreases and the saddle-nodes that are so characteristic of the snaking region are progressively eliminated. In particular, in the case shown in figure 6(*a*) the convectons grow in length by adding new cells on either side while the solution branch remains monotonic in Ra. The resulting *smooth snaking* (Dawes & Lilley 2010; Lo Jacono *et al.* 2011) can also be attributed to the presence of the conserved quantity $\bar{V}$.

3.4. *Localized states in the supercritical regime*

As σ is increased, the primary branch of periodic states becomes less and less subcritical and a transition occurs towards supercriticality. Figure 7(*a*) presents the bifurcation diagram for $\sigma = 0.6$ and $T = 40$ in a domain $\Gamma = 10\lambda_c$ where, at this Taylor number, the critical wavenumber $k_c \approx 4.0481$. For these parameter values the primary solution branch bifurcates supercritically at $Ra = Ra_c \approx 2068$. This branch loses stability almost immediately, at $Ra \approx 2073$, creating a pair of branches of spatially modulated states. These states behave in exactly the same way as in the subcritical case: as one follows the resulting $L_{10}^{\pm}$ towards smaller Rayleigh numbers the modulation strengthens and generates, by the time one reaches the leftmost saddle-nodes, isolated convectons of even and odd parity. Beyond this point the $L_{10}^{\pm}$ branches intertwine resulting in smooth snaking without any additional saddle-nodes until the rightmost saddle-nodes marking the right edge of the existence region for convectons

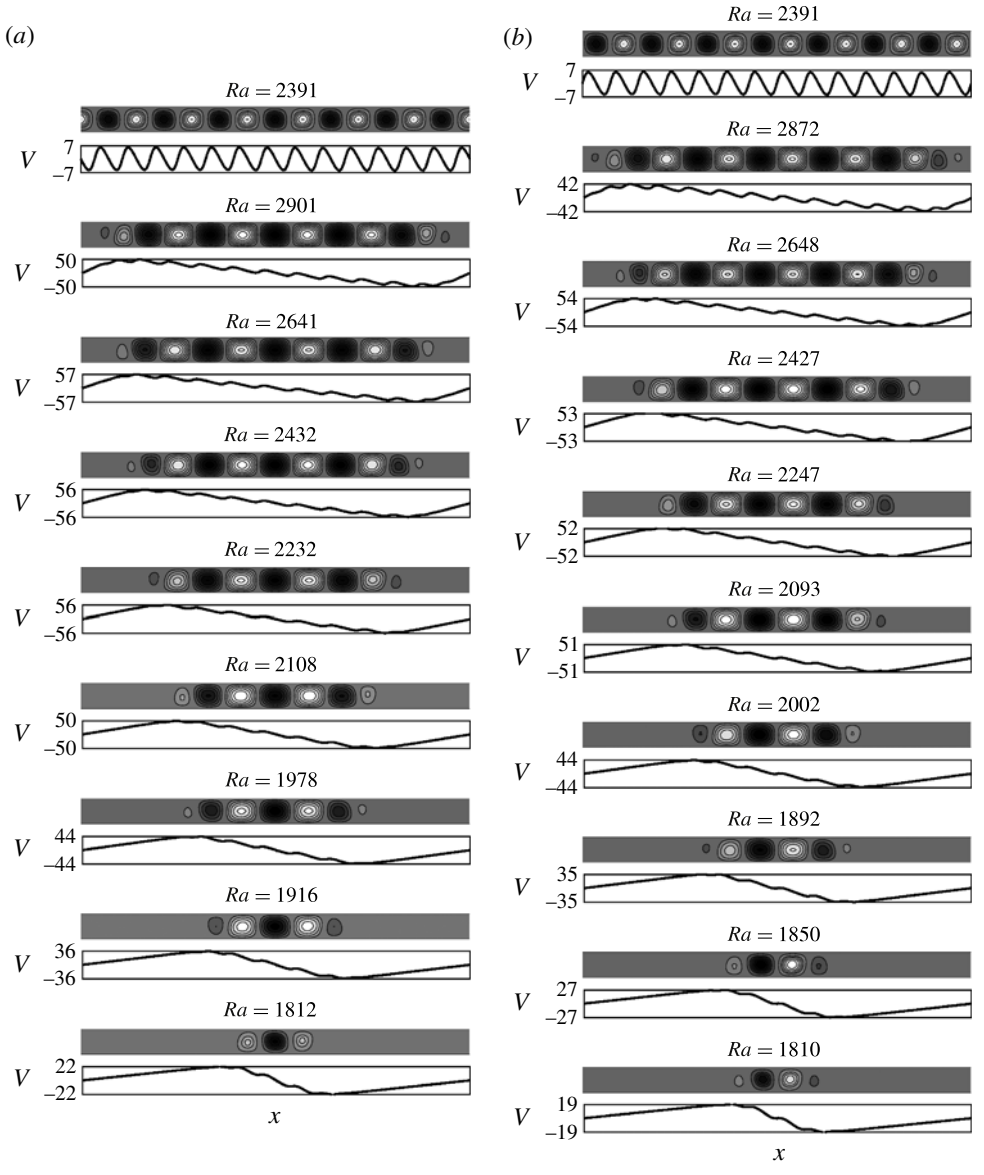

FIGURE 8. Same as figure 2 but for the localized solutions along (*a*) L_{10}^{-} and (*b*) L_{10}^{+} in figure 7(*a*).

(Dawes & Lilley 2010). In the present case both $L_{10}^{\pm}$ branches terminate together on the P_7 branch at $Ra \approx 2391$. Figure 8 shows the solutions along these branches using the same representation as used in figure 2. The solutions are qualitatively similar to those in figure 2 except for broader diffusive layers between adjacent cells owing to the larger Prandtl number. As a result the saw-tooth structure of $V(x)$ in the periodic state is less marked. However, the localized states are still accompanied by strong negative shear within the structure (figure 7*b*) that serves to reduce the local rotation rate, with a compensating prograde shear zone outside. Thus the convectons are embedded in a self-generated shear zone exactly as in the subcritical case.

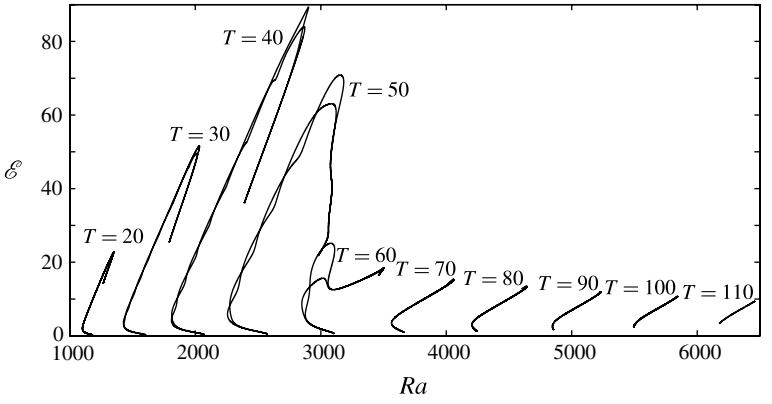

FIGURE 9. Bifurcation diagrams representing the average poloidal kinetic energy $\mathscr{E}$ as a function of the Rayleigh number Ra for the $L_{10}^{\pm}$ branches for different Taylor numbers T when $\sigma = 0.6$ and $\Gamma = 10\lambda_c$. In all cases these branches bifurcate from P_{10} (not shown). The $L_{10}^{\pm}$ branches are indistinguishable for $T \geqslant 70$.

In figure 9 we show the evolution of the $L_{10}^{\pm}$ branch as T is varied from $T = 20$ to $T = 110$, while keeping $\sigma = 0.6$ and $\Gamma = 10\lambda_c$. We emphasize again that λ_c depends on the value of T used. In all cases the primary periodic branch bifurcates supercritically. We see that for small T the extent of the subcriticality of the secondary branches is relatively narrow while the maximum energy along the branch remains relatively small. With increasing T the branch of localized states moves to larger values of Ra (along with the primary bifurcation). At the same time the branch becomes more subcritical and the maximum energy attained increases rapidly. Simultaneously the small-amplitude oscillations superposed on the general tilt of the branch become more and more noticeable although the snaking remains smooth. The number of these oscillations decreases with increasing T owing to two properties of the solutions: the Rayleigh number range for the presence of convectons increases with T and the wavelength within the convectons increases with Ra. As a result fewer and fewer cells can be added before the domain is filled and the $L_{10}^{\pm}$ branches must terminate. For example, L_{10}^{+} terminates on P_8 when $T = 20$ and on P_7 when $T = 30$ and $T = 40$. This fact is responsible for the observation that maximum energy is attained for $T \approx 40$ after which the energy begins to drop off. The extent in Rayleigh number within which convectons are present is likewise widest for $T \approx 40$ and starts to decrease for larger T while the extent of the subcriticality of the $L_{10}^{\pm}$ branches decreases at the same time, and essentially disappears by $T = 100$. Figure 10 shows the existence region of convectons in the (Ra, T) plane when $\sigma = 0.6$ and $\Gamma = 10\lambda_c$. The figure confirms that the range of Ra for which such states are present is broadest when $T \approx 40$ and that it shrinks to zero at both small and large T. For example, we have found no secondary bifurcations from the periodic state at $T = 5$ and $T = 120$. The localization of the lowest Rayleigh number convectons is likewise strongest at $T \approx 40$ (figure 11).

Figure 9 reveals another interesting aspect of this evolution. Until $T = 50$ the slope $\mathrm{d}\mathscr{E}/\mathrm{d}(Ra)$ is approximately constant and independent of T. This is so beyond $T = 60$ as well, although the slope now takes a significantly lower value. In the former regime the localized structures grow via nucleation of new cells, behaviour that is associated with snaking. In contrast, beyond $T = 60$ snaking is absent, suggesting that convectons

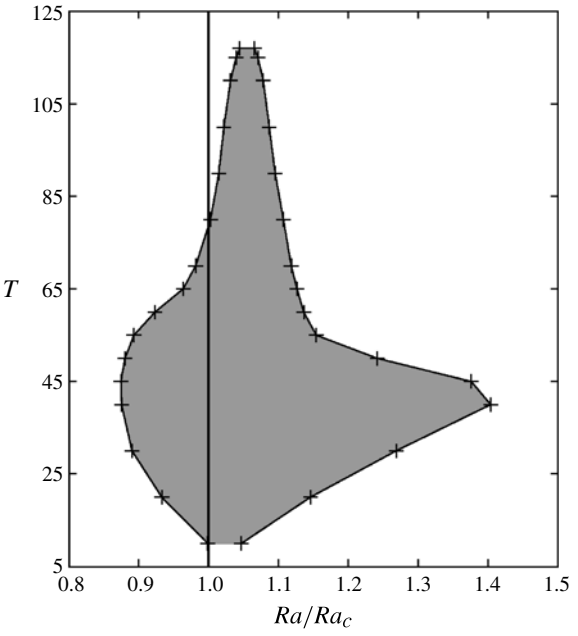

FIGURE 10. The existence region (shaded) of convectons in the (Ra, T) plane when $\sigma = 0.6$. The vertical line at $Ra = Ra_c$ represents the onset of spatially periodic convection. The existence region is delimited either by saddle-node bifurcations on the convecton branches, or by bifurcations to modulated states if no such saddle-nodes exist.

no longer grow via nucleation. Moreover, the solution branches in this regime always terminate on P_{10}. Figure 9 suggests that the transition between these two regimes takes place at approximately $T = 60$.

In an attempt to understand the origin of this change in behaviour we plot in figures 12 and 13 the profiles along the branches of even-parity convectons for $T = 50$ and $T = 100$. While the convectons are in both cases well localized near the left saddle-nodes (albeit less so when T is larger) the figures reveal a significant change in the wavelength of the cells comprising them. In figure 12 the cells are initially broad and remain so until maximum energy is reached; thereafter the wavelength decreases rapidly and the branch terminates on P_{10}. In contrast, the wavelength of the cells when $T = 100$ (figure 13) hardly changes as $\mathscr{E}$ increases from small values to large, and this is so already when $Ta = 70$. At the same time the dimples representing nucleation events in figure 12 shrink and the convecton branches become indistinguishable. A similar transition was recently observed in magnetoconvection with an imposed vertical magnetic field (Lo Jacono *et al.* 2011; Lo Jacono, Bergeon & Knobloch 2012). We surmise that the sudden change in slope of the slanted snaking that takes place around $T = 60$ is related to this change in cell wavelength and note, in particular, that broader cells are more efficient at transporting heat since in narrower cells such as those favoured at larger rotation rates the rising plumes exchange more heat with falling plumes, thereby reducing their efficiency and hence the associated Nusselt number. Thus for $T \lesssim 50$ the length scale of convection is selected primarily by thermal effects, while for $T \gtrsim 70$ the length scale is selected primarily by a competition between the tendency towards a Taylor–Proudman balance

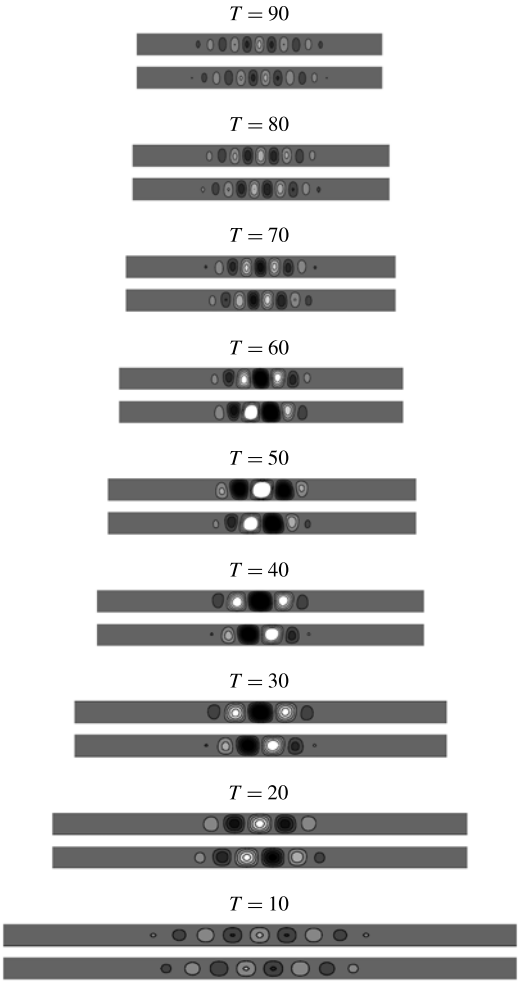

FIGURE 11. Localized solutions at the leftmost saddle-node for T increasing from 10 to 90 in steps of 10 when $\sigma = 0.6$ and $\Gamma = 10\lambda_c$. The same isovalues of the streamfunction are used in all panels. The localization is strongest when $T \approx 40$.

and the requirement that the flow transport heat at the level specified by the Rayleigh number. In the former regime localization is strong and nucleation of new cells occurs at well-defined Rayleigh numbers. In contrast, the latter regime is characterized by weak localization while new cells grow gradually over a range of Rayleigh numbers. Of course, for $T \lesssim 10$ localization is also weak but this is a consequence of the slow rotation rate.

Figures 2 and 8 also reveal a systematic trend that merits explanation: the convecton cells are always broader than the corresponding cells in the periodic state. We believe that this is a reflection of the shear V' across the convecton. If we suppose that this shear is smoothed out and is a linear function of x, i.e. $V(x) = sx$, where $s < 0$ (see e.g. figure 2) we may include this shear in the base state and study the stability of the state $(\psi, \theta, v) = (0, 0, sx)$ instead of the state $(\psi, \theta, v) = (0, 0, 0)$. The stability of this state is described by the relations given in § 4 with T^2 replaced by $T(T + \sigma^{-1}s)$. It

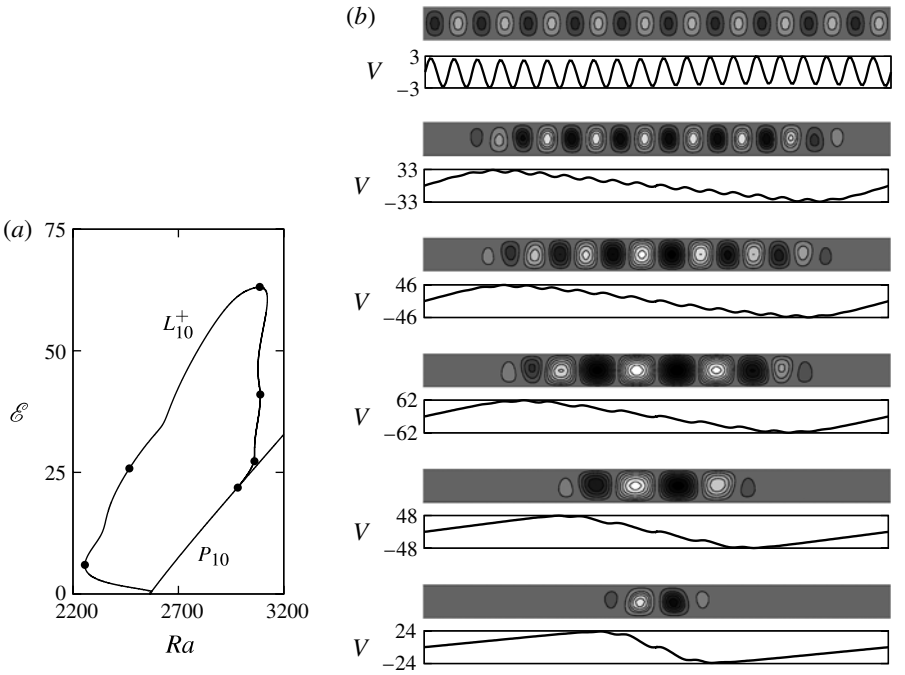

FIGURE 12. (*a*) Bifurcation diagram for the L_{10}^{+} branch when $T = 50$ (figure 9). The branch bifurcates from P_{10} and terminates on P_{10}. The solid dots indicate the location of the solutions shown in (*b*) starting from the left saddle-node (bottom panel) and ending on the periodic state P_{10} (top panel).

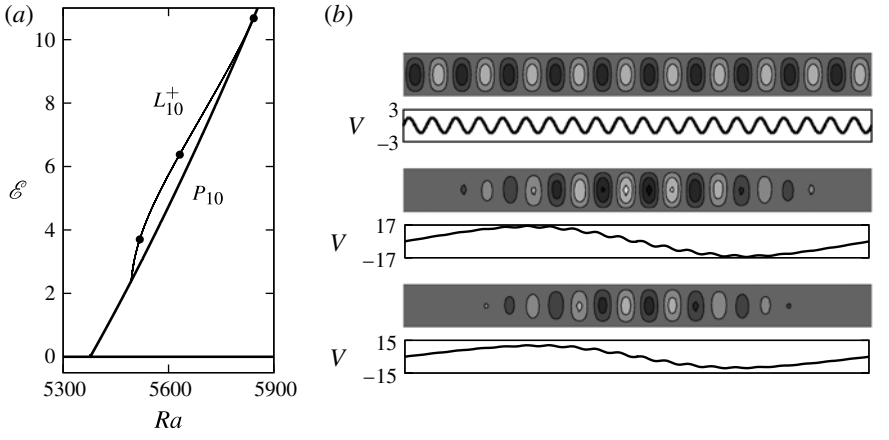

FIGURE 13. As for figure 12 but for $T = 100$.

follows that negative shear ($s < 0$) decreases both the critical Rayleigh number Ra_c and the associated critical wavenumber k_c relative to the case $s = 0$. However, this linear effect is quickly overwhelmed by the nonlinear wavelength change that takes place with increasing amplitude. We return to this question in the next section.

4. Theoretical understanding of the bifurcation to convectons

Linear stability analysis predicts that the conduction state $\psi = \theta = v = 0$ loses stability with respect to stationary perturbations with wavenumber k when Ra reaches

$$Ra(k) = \frac{p^3+\pi^2 T^2}{k^2}, \quad p \equiv k^2+\pi^2. \tag{4.1}$$

The critical value Ra_c is defined as the minimum of $Ra(k)$ for a stationary bifurcation to occur, implying that (Veronis 1959)

$$Ra_c = 3p_c^2, \quad p_c^2(2k_c^2-\pi^2) = T^2\pi^2, \tag{4.2}$$

where $p_c \equiv k_c^2+\pi^2$, and $k_c = k_c(T)$ is the critical wavenumber satisfying the second of the above relations. In the following we omit the subscript on k_c and p_c but retain the subscript on $Ra_c \equiv Ra_c(T)$.

To compute the resulting solutions in the weakly nonlinear regime we suppose that $Ra = Ra_c + \epsilon^2 r$, where $r = O(1)$, $\epsilon \ll 1$, and introduce a large spatial scale $X = \epsilon x$ and a slow time scale $T_2 = \epsilon^2 t$. We follow Cox & Matthews (2001) and look for solutions in the form

$$\psi = \frac{\epsilon}{2}\left(a(X,T_2)\mathrm{e}^{\mathrm{i}kx} + \text{c.c.}\right)\sin(\pi z) + \text{h.o.t.}, \tag{4.3}$$

$$\theta = \frac{\epsilon k}{2p}\left(\mathrm{i}a(X,T_2)\mathrm{e}^{\mathrm{i}kx} + \text{c.c.}\right)\sin(\pi z) + \text{h.o.t.}, \tag{4.4}$$

$$v = \epsilon V(X,T_2) + \frac{\epsilon T\pi}{2p}\left(a(X,T_2)\mathrm{e}^{\mathrm{i}kx} + \text{c.c.}\right)\cos(\pi z) + \text{h.o.t.} \tag{4.5}$$

The large-scale zonal velocity V is necessary to capture the shear that builds up across a convecton and enters at $O(\epsilon)$; its inclusion is a consequence of the phase-like quality of the variable v, i.e. the invariance of (2.1)–(2.3) with the boundary conditions (2.5) with respect to $v \to v+c$, where c is a constant. At third-order we obtain the equations (Cox & Matthews 2001)

$$\frac{p(3k^2\sigma - k^2 + 2\pi^2)}{\sigma k^2}a_{T_2} = ra + 12pa_{XX} - \frac{3pk^2}{8}(1-\xi^2)|a|^2 a - \frac{T\pi^2}{\sigma k^2}aV_X, \tag{4.6}$$

$$V_{T_2} = \sigma V_{XX} + \frac{T\pi^2}{4p}(|a|^2)_X, \tag{4.7}$$

where $\xi \equiv T\pi^2/\sqrt{3}pk^2\sigma$. This set of equations can be further simplified by rescaling the variables ($a \to 2A/\sqrt{3p}k$, $V \to 2V/\sqrt{p}$, $X \to \sqrt{12p}X$, $T_2 \to 12pT_2/\sigma$), leading to

$$\eta A_{T_2} = rA + A_{XX} - \frac{1-\xi^2}{2}|A|^2 A - \xi AV_X, \tag{4.8}$$

$$V_{T_2} = V_{XX} + \xi\,(|A|^2)_X, \tag{4.9}$$

where $\eta \equiv (3k^2\sigma - k^2 + 2\pi^2)/12k^2$. The quantity η vanishes at the Takens–Bogdanov point $Ra_H = Ra_c$ where Ra_H is the critical Rayleigh number for the onset of a Hopf mode with the same wavenumber k. In the present work we are interested in the case in which the conduction state loses stability at a steady-state bifurcation, i.e. a Hopf bifurcation is absent. In this case $\eta > 0$.

Equations (4.8) and (4.9) can also be written in the form

$$A_{T_2} = -\eta^{-1}\frac{\delta F}{\delta A^*}, \quad V_{T_2} = -\frac{\delta F}{\delta V}, \tag{4.10}$$

where F is defined as

$$F[A, A^*, V] = \int_{\Gamma'} \left\{ -r\,|A|^2 + |A_X|^2 + \frac{1}{2}{V_X}^2 + \frac{1-\xi^2}{4}\,|A|^4 + \xi\,|A|^2\,V_X \right\} \mathrm{d}X. \tag{4.11}$$

Here Γ' is the period Γ on the scale X. The functional $F[A, A^*, V]$ is bounded from below when $\xi^2 < 1/3$. It follows that in this case the system (4.6)–(4.7) has variational dynamics provided only that $\eta > 0$. This is not necessarily the case for the original system (2.1)–(2.3).

In the stationary case with PBC on the large spatial scale X (4.9) implies that

$$V_X = \xi\left(\langle |A|^2\rangle - |A|^2\right), \tag{4.12}$$

where $\langle\cdot\rangle$ represents a spatial average over the domain. Thus $V_X > 0$ if $|A|^2 < \langle |A|^2\rangle$, i.e. outside the convecton, while $V_X < 0$ if $|A|^2 > \langle |A|^2\rangle$, i.e. inside the convecton, exactly as found in figures 2 and 8. Moreover, using (4.12) to eliminate V_X from (4.8) we obtain the *non-local* equation (Cox & Matthews 2001)

$$rA + A_{XX} - \tfrac{1}{2}(1-3\xi^2)\,|A|^2 A - \xi^2\langle |A|^2\rangle A = 0. \tag{4.13}$$

Let $A = \rho e^{i\phi}$ with $\rho, \phi \in \mathbb{R}$ and $\rho > 0$. If ρ is independent of X, i.e. the solution is periodic, then $\langle |A|^2\rangle = \rho^2 = 2(r-q^2)/(1-\xi^2)$, where $q \equiv \phi_X$, and the solution is supercritical when $\xi^2 - 1 < 0$ and subcritical when $\xi^2 - 1 > 0$, as determined already by Veronis (1959). The point $\xi^2 = 1$, sometimes called the tricritical point, occurs at

$$T_c = \frac{\sqrt{3}\sigma\pi^2\left(2 \pm \sqrt{1-3\sigma^2}\right)}{\left(1 \pm \sqrt{1-3\sigma^2}\right)^2} \equiv T_{\pm}^{per}. \tag{4.14}$$

This relation implies that, provided $\sigma < 1/\sqrt{3}$, the bifurcation to periodic convection is supercritical for $T < T_+^{per}$, becomes subcritical for $T_+^{per} < T < T_-^{per}$ and then changes back to supercritical for $T > T_-^{per}$, cf. Goldstein *et al.* (1990); the bifurcation is always supercritical when $\sigma \geqslant 1/\sqrt{3}$. Equation (4.12) shows that the inclusion of amplitude modulation on the scale $X = O(1)$ alters this picture dramatically. In particular, the codimension-two point for modulated wavetrains occurs at a different location, as determined next. This shift is a consequence of the nonlinear interaction between the unstable mode and the marginally stable long-wave mode V.

Non-local equations of the form (4.13) have been studied before (Hall 1984; Elmer 1988; Norbury, Wei & Winter 2002; Vega 2005; Norbury, Wei & Winter 2007). We summarize first the stability properties of the periodic solution $A = \rho e^{iqX}$, $V = 0$, corresponding to a wavetrain (ψ, θ, v) with wavenumber $k + \epsilon q$. We write $A = \rho e^{iqX}(1 + \tilde{A})$, where $|\tilde{A}| \ll 1$, and let V be the associated zonal velocity perturbation. The linearized equations are

$$\eta\tilde{A}_{T_2} = \tilde{A}_{XX} + 2iq\tilde{A}_X - (1-\xi^2)\rho^2 \mathrm{Re}[\tilde{A}] - \xi V_X, \tag{4.15}$$

$$V_{T_2} = V_{XX} + 2\xi\rho^2 \mathrm{Re}\,[\tilde{A}]_X\,. \tag{4.16}$$

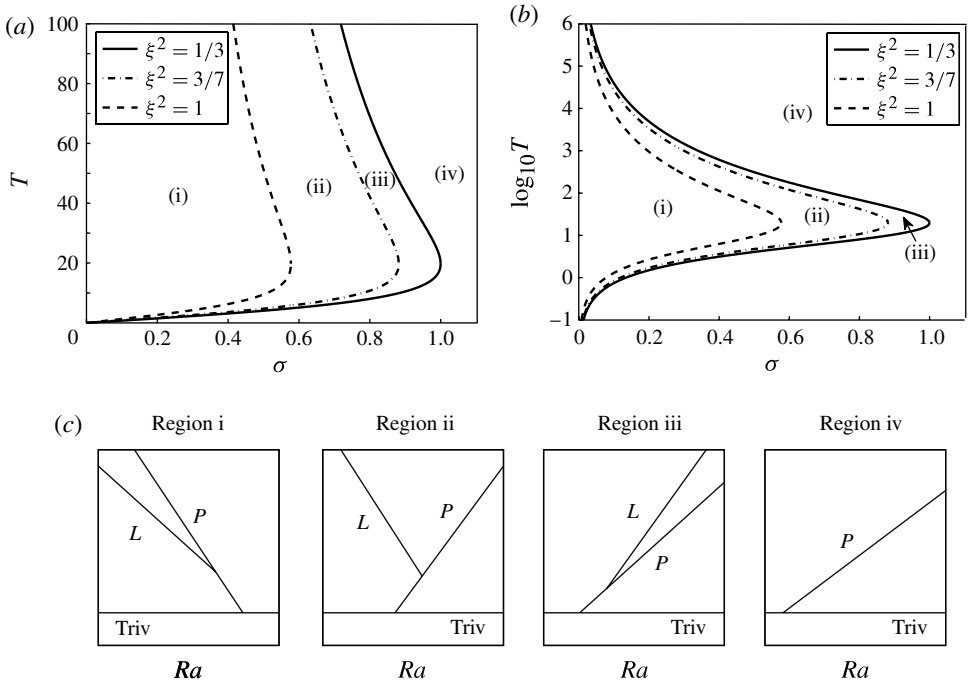

FIGURE 14. Regions of super- and subcriticality for primary–secondary branches in the (σ, T) plane on (*a*) linear and (*b*) logarithmic scales. (*c*) Sketches of the bifurcation diagrams characteristic of each of the four regions i–iv shown in (*a,b*). The curves $\xi^2 = 1$ and $\xi^2 = 1/3$ were computed by Cox & Matthews (2001).

The characteristic polynomial for the growth rate λ of a Fourier mode with wavenumber l is (Cox & Matthews 2001)

$$\eta^2\lambda^3 + \eta\lambda^2[(1-\xi^2)\rho^2 + (2+\eta)l^2] + \lambda l^2[(1-\xi^2)\rho^2 + \eta(1-3\xi^2)\rho^2 - 4q^2] + \lambda l^4(1+2\eta) + l^4[l^2 - 4q^2 + (1-3\xi^2)\rho^2] = 0. \tag{4.17}$$

Thus when $|l| \ll 1$ there is a pure amplitude mode with $O(1)$ eigenvalue $\lambda \approx (\xi^2 - 1)\rho^2/\eta + O(l^2)$ reflecting the supercriticality or subcriticality of the periodic state and two $O(l^2)$ eigenvalues satisfying

$$\eta\rho^2(1-\xi^2)\lambda^2 + [\eta\rho^2(1-3\xi^2) + \rho^2(1-\xi^2) - 4q^2]l^2\lambda + [\rho^2(1-3\xi^2) - 4q^2]l^4 \approx 0. \tag{4.18}$$

It follows that when $q = 0$ there are two long-wave modes, $\lambda = -l^2/\eta$ and $\lambda = ((3\xi^2 - 1)/(1 - \xi^2))l^2$. Thus when $\eta < 0$ ($Ra_H < Ra_c$) the periodic state at band centre is necessarily unstable. On the other hand when $\eta > 0$ (no primary Hopf bifurcation) there is a long-wave instability when $1/3 < \xi^2 < 1$ but no long-wave instability when $\xi^2 < 1/3$. Thus the $q = 0$ mode becomes unstable as ξ^2 decreases through $\xi^2 = 1/3$, i.e. as the rotation increases *or* decreases (see figure 14). The resulting instability generates an amplitude modulated wavetrain. When $\xi^2 > 1$ the periodic state is subcritical and therefore also unstable. Finally, when $q \neq 0$ the two long-wave modes become coupled but no secondary Hopf bifurcation is possible

when $\eta > 0$. These results apply to infinite domains; in finite domains they require modification as discussed further below (Norbury *et al.* 2007).

The spatial dynamics of (4.13) take the form of a complex Duffing equation which is integrable with two conserved quantities:

$$K_1 \equiv \rho^2 \phi_X, \quad K_2 \equiv \tfrac{1}{2}(\rho_X)^2 + U[\rho], \tag{4.19}$$

where

$$U[\rho] \equiv \frac{1}{2} r' \rho^2 + \frac{K_1^2}{2\rho^2} - \frac{1}{8}(1 - 3\xi^2)\rho^4. \tag{4.20}$$

Here $r' \equiv r - \xi^2 \langle \rho^2 \rangle$, implying that the bifurcation parameter r is increasingly modified as the convection amplitude ρ grows. In a periodic domain with period Γ' PBC and the integral constraint imply

$$\frac{\Gamma'}{2n} = \int_{\rho_{min}}^{\rho_{max}} \frac{\mathrm{d}\rho}{\sqrt{2(K_2 - U)}}, \quad \frac{\langle \rho^2 \rangle \Gamma'}{2n} = \int_{\rho_{min}}^{\rho_{max}} \frac{\rho^2 \,\mathrm{d}\rho}{\sqrt{2(K_2 - U)}}, \tag{4.21}$$

where $n \in \mathbb{N}$ is the number of full periods of amplitude modulation within Γ', and ρ_{min} (ρ_{max}) corresponds to the minimum (maximum) of ρ during amplitude modulation. The total change of phase across the domain (including the contribution from the fast oscillation with wavenumber k) must be an integer multiple of 2π implying that $\int_0^{\Gamma'} \phi_X \,\mathrm{d}X$ must also be a constant unless a phase jump occurs. The wavenumber $q \equiv \phi_X$ is a constant along the branch of periodic states. Secondary branching occurs when ρ attains a local minimum of U. To fit PBC, $U_{\rho\rho}$ must be equal to $4\pi^2 n^2 / \Gamma'^2$ which occurs at $r = r_n$ where

$$r_n \equiv \frac{2\pi^2 n^2}{\Gamma'^2} \frac{1 - \xi^2}{3\xi^2 - 1} + \frac{5\xi^2 - 3}{3\xi^2 - 1} q^2 \tag{4.22}$$

in both super- and subcritical cases. When q is small, a secondary bifurcation is only possible when $\xi^2 > 1/3$. The branching direction at these points was calculated by Elmer (1988), who shows that when $q = 0$, the secondary bifurcation is supercritical when $\xi^2 < 3/7$ and subcritical when $\xi^2 > 3/7$ (see the Appendix for an alternative derivation of this result). In summary, there are four possible scenarios for the primary–secondary bifurcations with PBC: (i) both bifurcations are subcritical ($\xi^2 > 1$); (ii) the primary bifurcation is supercritical while the secondary bifurcation is subcritical ($3/7 < \xi^2 < 1$); (iii) both bifurcations are supercritical ($1/3 < \xi^2 < 3/7$); and (iv) the primary bifurcation is supercritical but no secondary bifurcation is present ($\xi^2 < 1/3$). Figure 14 shows the regions of super- and subcriticality in the (σ, T) plane, while figure 15 shows sample bifurcation diagrams computed from (4.13) for (some of) the Taylor numbers used in figure 9 using the numerical continuation software AUTO (Doedel *et al.* 2008). Owing to translation symmetry ($A \to A\mathrm{e}^{\mathrm{i}\phi_0}$) and spatial reversibility ($A \to A^*$, $X \to -X$), we perform continuation on the half-domain using Neumann boundary conditions (NBC), i.e.

$$\mathrm{Re}[A_X] = \mathrm{Im}[A] = 0 \tag{4.23}$$

at the boundaries. The average poloidal kinetic energy $\mathscr{E}$ to $O(\epsilon^4)$ takes the form

$$\mathscr{E} = \tfrac{1}{8}\epsilon^2 p \langle |a|^2 \rangle + \tfrac{1}{8}\mathrm{i}\epsilon^3 k \langle a a_X^* - a^* a_X \rangle + \tfrac{1}{8}\epsilon^4 \langle |a_X|^2 \rangle, \tag{4.24}$$

where the amplitude a is defined in (4.3). We use this expression to draw bifurcation diagrams $\mathscr{E}(Ra)$ for $\sigma = 0.6$. For this purpose we define ϵ using the ratio of the

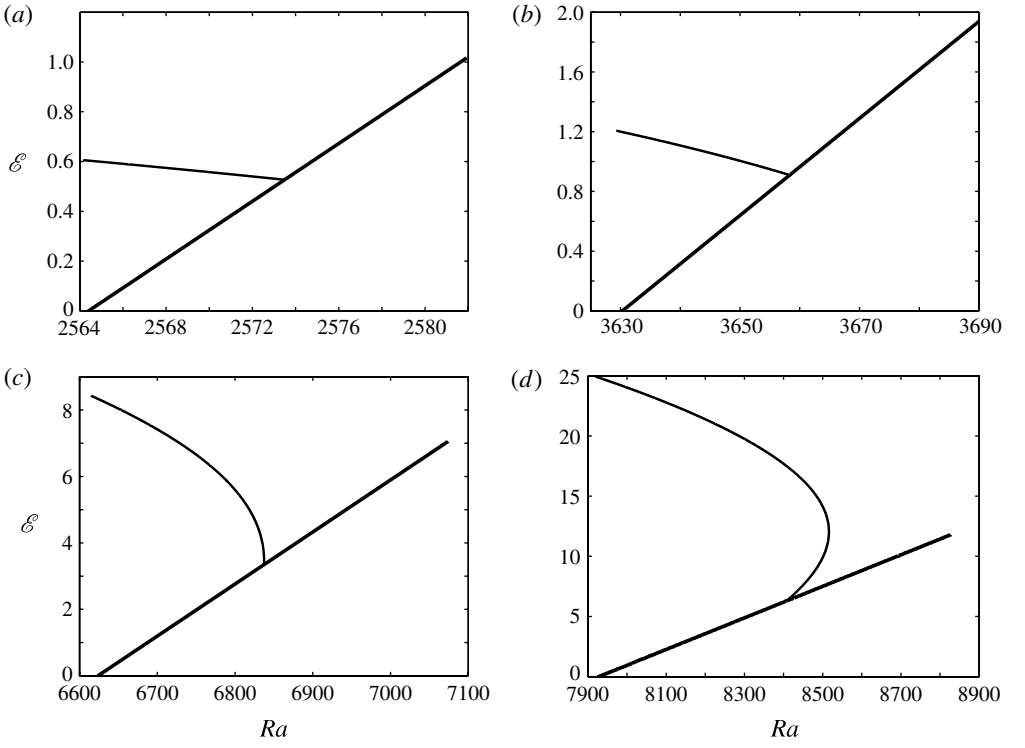

FIGURE 15. Bifurcation diagrams showing stationary solutions of (4.13) with $\phi_X = 0$ satisfying NBC for $\sigma = 0.6$ and $\Gamma = 10\lambda_c$. Thick solid lines: primary state (periodic convection). Thin solid lines: modulated states (convectons). (*a*) $T = 50$ ($\xi^2 = 0.7032$, region ii). (*b*) $T = 70$ ($\xi^2 = 0.5882$, region ii). (*c*) $T = 120$ ($\xi^2 = 0.4269$, region ii). (*d*) $T = 140$ ($\xi^2 = 0.3877$, region iii). The periodic state is stable up to the secondary bifurcation; in (*d*) the modulated state is stable up to the saddle-node.

small and large scales, $\epsilon \equiv \lambda_c/\Gamma = 0.1$. We then solve (4.13) in the domain $\Gamma' = 2\pi/k$ varying the parameter r. Owing to the relatively small domain (large value of ϵ) the calculation requires quite large values of r in order to locate the secondary states. The resulting energy $\mathscr{E}$ is therefore also large. Of course, as r and hence $\mathscr{E}$ increase the amplitude equation (4.13) becomes less reliable, and comparison with the results of § 3 shows that in the full problem the convecton branch always turns towards larger values of Ra as $\mathscr{E}$ increases, in contrast to the predictions summarized below.

Figure 15 shows that for $\sigma = 0.6$ the convecton branch bifurcates supercritically from the periodic states once $T \geqslant 119.2579$ (i.e. $\xi^2 < 3/7$), in reasonable agreement with figure 9. The bifurcation to convectons is also supercritical when $T < 6.1108$ since for these values $\xi^2 < 3/7$ also. As ξ^2 decreases towards $\xi^2 = 1/3$ the secondary bifurcation moves to larger and larger amplitude and for $\xi^2 < 1/3$ the secondary bifurcation to convectons is absent. Of course before this happens (4.13) loses validity, a fact that may account for the discrepancy between figure 15(*d*) and the phase diagram in figure 10; in particular, a different scaling is required to understand the disappearance of the convecton branch (see § 5).

We define the length L of a convecton as the interval where $|A|^2 > \langle |A|^2 \rangle$. This interval can be calculated explicitly by solving the non-local equation (4.13) in terms

of elliptic functions. The explicit form of the $n = 1$ solution is

$$\rho^2/\rho_+^2 = 1 - \zeta^2 \mathrm{sn}^2\left[\tfrac{1}{2}\sqrt{\rho_+^2(3\xi^2-1)}X;\,\zeta\right], \tag{4.25}$$

where

$$\Gamma' = \frac{4K(\zeta)}{\sqrt{\rho_+^2(3\xi^2-1)}}, \quad \langle\rho^2\rangle = \frac{E(\zeta)}{K(\zeta)}\rho_+^2. \tag{4.26}$$

The ratio L/Γ' is thus equal to $F(\zeta^{-1}\sqrt{1-E(\zeta)/K(\zeta)},\zeta)/K(\zeta)$. Here $\zeta \equiv \sqrt{1-\rho_-^2/\rho_+^2}$, $\rho_\pm$ are the positive roots of $U[\rho] = K_2$ with $\rho_- < \rho_+$, F is the incomplete elliptic integral of the first kind, and K and E are the complete elliptic integrals of the first and second kind. There are two limiting regimes which yield simple predictions for the parameter dependence of L. In the case of weak spatial modulation, K_2 is only slightly greater than the local minimum of U and we have

$$\frac{L}{\Gamma'} = \frac{1}{2} - \frac{\Gamma'}{2\pi^2}\sqrt{\frac{(3\xi^2-1)(r-r_1)}{3-7\xi^2}} + O(|r-r_1|). \tag{4.27}$$

In the strongly modulated case with large domain size ($\Gamma'\sqrt{-r'} \gg 1$), the solutions with $\phi_X = 0$ can be approximated by the sech function (Matthews & Cox 2000; Cox & Matthews 2001),

$$\rho = \sqrt{\frac{-4r'}{3\xi^2-1}}\,\mathrm{sech}\left(\sqrt{-r'}X\right), \tag{4.28}$$

where

$$r' = -\tilde{r}\left(1 \pm \sqrt{1-\frac{r}{\tilde{r}}}\right)^2, \quad r < \tilde{r} \equiv \frac{16\xi^4}{\Gamma'^2\,(3\xi^2-1)^2};$$

the $+$ solution exists for all $r < \tilde{r}$ while the $-$ solution exists for $0 < r < \tilde{r}$ only. The resulting solutions are homoclinic to $\rho = 0$ and so represent fully localized convectons. It should be noted that due to finite domain size, $\langle\rho^2\rangle$ is non-zero. The length of such a convecton is thus

$$\frac{L}{\Gamma'} \approx \frac{\log(2\Gamma'\sqrt{-r'})}{\Gamma'\sqrt{-r'}}. \tag{4.29}$$

See Proctor (2001) and Cox (2004) for related results.

The stability of the solutions (4.25) on a finite domain was studied rigorously by Norbury *et al.* (2007) in the case $\eta > 0$. In conjunction with the Appendix these results confirm that for $1/3 < \xi^2 < 3/7$ the secondary branch is supercritical and stable in the interval between the bifurcation point and a saddle-node on the right and unstable thereafter. For $\xi^2 > 3/7$ the secondary branch is subcritical and unstable throughout (figure 15).

We can use the above results to calculate the local shear at the maximum of the amplitude modulation. For the $n = 1$ secondary branch we obtain

$$s = -\frac{8T\pi^3}{3p^2k^2\sigma\Gamma}\sqrt{\frac{Ra-Ra_1}{(3\xi^2-1)(3-7\xi^2)}} + O(|Ra-Ra_1|), \tag{4.30}$$

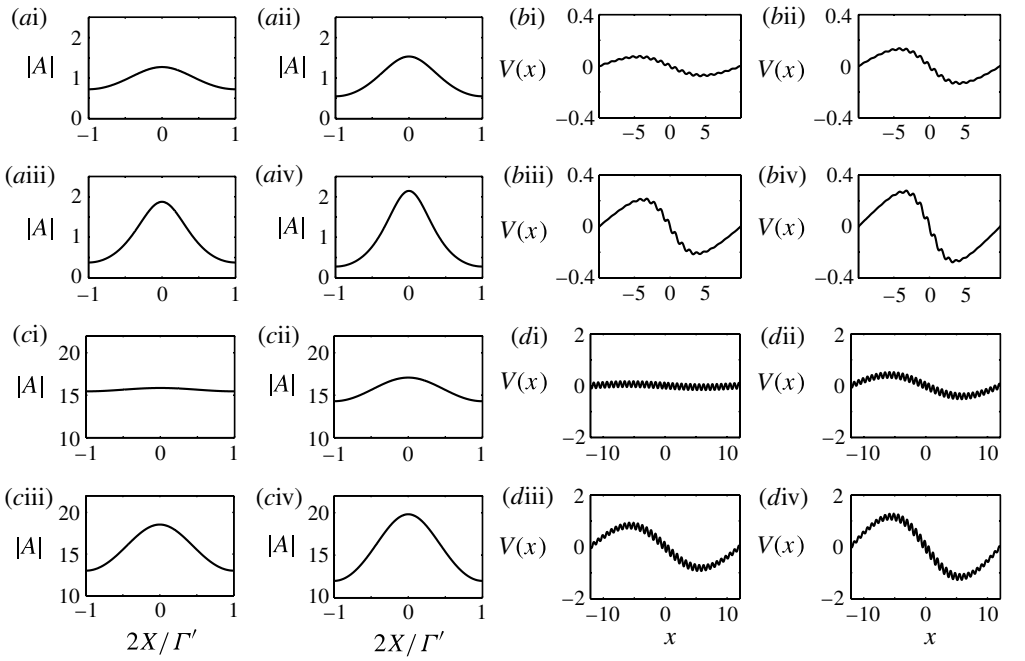

FIGURE 16. Sample profiles of the stationary solutions of (4.13) when $\Gamma = 10\lambda_c$. The amplitude $|A|$ is shown as function of a scaled variable while the z-average of the zonal velocity, $V(x)$ defined in (3.2), is shown in terms of the original variable x. (*a*,*b*) $\sigma = 0.1$, $T = 20$ ($\xi^2 = 33.3308$). (i) $Ra = 1174.3$. (ii) $Ra = 1171.8$. (iii) $Ra = 1166.8$. (iv) $Ra = 1161.7$. (*c*,*d*) $\sigma = 0.6$, $T = 50$ ($\xi^2 = 0.7032$). (i) $Ra = 2573.5$. (ii) $Ra = 2573.3$. (iii) $Ra = 2572.6$. (iv) $Ra = 2571.6$. Note that the spatial frequency of $V(x)$ is double that of $\psi(x)$.

where $Ra = Ra_1$ denotes the location of the secondary bifurcation. To obtain this result we include a non-zero constant of integration in (3.3), as required by PBC, and choose this constant to cancel the mean Reynolds stress associated with periodic wavetrains. With this shear the critical wavenumber $\tilde{k}_c$ for instability of the sheared base state $(\psi, \theta, v) = (0, 0, sx)$ differs from k_c in (4.2) by

$$\tilde{k}_c - k_c \approx \frac{T\pi^2 s}{12pk^3\sigma} = -\frac{2T^2\pi^5}{9p^3k^5\sigma^2\Gamma}\sqrt{\frac{Ra - Ra_1}{(3\xi^2 - 1)(3 - 7\xi^2)}} + O(|Ra - Ra_1|), \quad (4.31)$$

showing that the wavelength of the instability of the sheared state will be larger than that of the unsheared state $(\psi, \theta, v) = (0, 0, 0)$. Numerical measurements of the convecton wavelength near onset (not shown) are consistent with the predicted square-root behaviour.

Figure 16(*a*,*b*) shows the profiles of the resulting convectons for $\xi^2 > 1$ (the subcritical case) and figure 16(*c*,*d*) for $\xi^2 < 1$ (the supercritical case). The results are in excellent qualitative agreement with the continuation results in figures 2 and 8.

5. The transition at $\xi^2 = 1/3$

The calculation in the preceding section shows that periodic wavetrains are supercritical for $\xi^2 < 1$ while spatially modulated wavetrains are present when $\xi^2 > 1/3$. Near these critical parameter values the amplitude equation (4.13) breaks

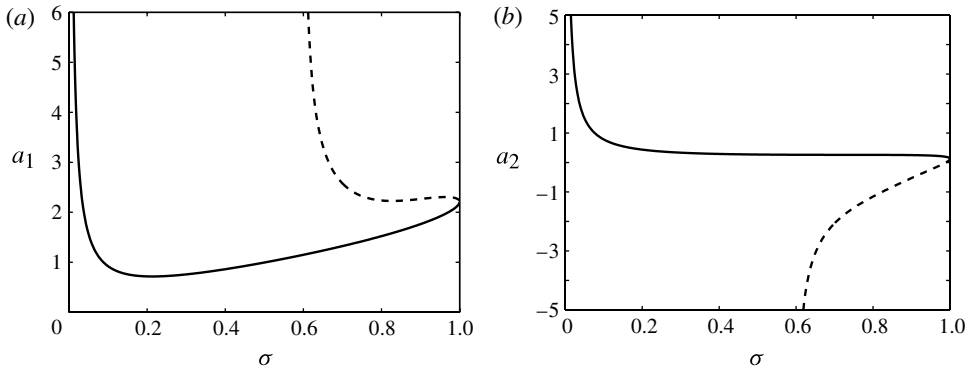

FIGURE 17. The coefficients (*a*) a_1 and (*b*) a_2 as functions of σ. Solid line: $T = T_+^{mod}$. Dashed line: $T = T_-^{mod}$.

down and the derivation must be extended to higher order. We focus here on the latter and more interesting case. To derive the corresponding amplitude equation we introduce a slow spatial variable $X \equiv \epsilon^2 x$, where $\epsilon \ll 1$, and write

$$\psi \sim \sum_{n=1}^{\infty} \epsilon^n \psi_n(x, X, z), \quad \theta \sim \sum_{n=1}^{\infty} \epsilon^n \theta_n(x, X, z), \quad v \sim v_0(X) + \sum_{n=1}^{\infty} \epsilon^n v_n(x, X, z). \quad (5.1)$$

In contrast to § 4 the leading-order term in the zonal velocity is now of order one. The parameters Ra and T are expanded as $Ra = Ra_c + \epsilon^2 r_2 + \epsilon^4 r_4$ and $T = T_c + \epsilon^2 \delta$, where Ra_c is the critical Rayleigh number for the onset of stationary convection and T_c is the critical Taylor number determined by $\xi^2 = 1/3$. Thus

$$T_c = T_\pm^{mod} \equiv \frac{\sigma \pi^2 (2 \pm \sqrt{1-\sigma^2})}{(1 \pm \sqrt{1-\sigma^2})^2} \quad (5.2)$$

and secondary bifurcations to modulated wavetrains occur in the interval $T_+^{mod} < T < T_-^{mod}$ ($\xi^2 > 1/3$) provided that $\sigma \leqslant 1$.

The expansion procedure leads to a non-local fifth-order stationary Ginzburg–Landau equation of the form (see supplementary material available at http://dx.doi.org/10.1017/jfm.2012.585 for this paper)

$$\mu A + A_{XX} + \mathrm{i}(\gamma A_X + a_1 |A|^2 A_X + a_2 A^2 A_X^*) + b |A|^2 A - |A|^4 A = 0, \quad (5.3)$$

where

$$\mu = \mu_0 + \mu_1 \langle |A|^2 \rangle + \mu_2 \langle |A|^4 \rangle + \mu_3 \mathrm{Im}[\langle A A_X^* \rangle] + \mu_4 \langle |A|^2 \rangle^2, \quad (5.4)$$

$$\gamma = \gamma_0 + \gamma_1 \langle |A|^2 \rangle, \quad b = b_0 + b_1 \langle |A|^2 \rangle. \quad (5.5)$$

Here $A(X)$ is a suitably scaled amplitude of the leading-order mode ψ_1. This equation generalizes (4.13) and applies whenever the coefficient of $|A|^4 A$ can be scaled to -1. This is always the case when $T_c = T_+^{mod}$ but when $T_c = T_-^{mod}$ the Prandtl number is restricted to the range $0.59796 \lesssim \sigma < 1$. These results and the coefficients $\mu_0, \ldots$ are readily deduced from the expressions provided in the supplementary material. Figure 17 shows the coefficients a_1 and a_2 as functions of σ.

An equation of the form (5.3) has been written down before (Elmer 1992; Riecke 1999) but its properties have not been studied except in one special case (Wei & Winter 2004). In contrast, the local version of the equation is well studied (Eckhaus & Iooss 1989; Kao & Knobloch 2012). We describe here the solutions of (5.3) for the parameter values used in § 3 and compare the results with the computed solutions of (2.1)–(2.3) with the boundary conditions (2.5).

We begin by observing that (5.3) with the non-local terms (5.5) is integrable just like (4.13), with the conserved quantities

$$K_1 = \rho^2\phi_X + \tfrac{1}{2}\gamma\rho^2 + \tfrac{1}{4}(a_1+a_2)\rho^4, \quad K_2 = \tfrac{1}{2}(\rho_X)^2 + U[\rho], \tag{5.6}$$

where

$$U[\rho] = \frac{K_1^2}{2\rho^2} + \left[\mu + \frac{\gamma^2}{4} + \frac{(3a_2-a_1)K_1}{2}\right]\frac{\rho^2}{2} + \left[b - \frac{\gamma(a_2-a_1)}{2}\right]\frac{\rho^4}{4} - \left[1 + \frac{(a_1+a_2)(5a_2-3a_1)}{16}\right]\frac{\rho^6}{6}.$$

For stationary solutions with $A_X = 0$, the amplitude ρ can be written as

$$\rho^2 = \rho_\pm^2 \equiv \frac{\mu_1 + b_0 \pm \sqrt{(\mu_1+b_0)^2 + 4\mu_0(1-b_1-\mu_2-\mu_4)}}{2(1-b_1-\mu_2-\mu_4)}. \tag{5.7}$$

The parameter values must lie in a range such that $\rho_\pm > 0$ is well defined. Secondary branching points depend on the sign of $U_{\rho\rho}$ at the stationary point $U_\rho = 0$ (Kao & Knobloch 2012). When $A_X = 0$ we have

$$U_{\rho\rho} = \gamma_0^2 + 2[b_0 + \gamma_0(a_1+\gamma_1)]\rho^2 + [(\gamma_1+a_1)^2 + 2b_1 - a_2^2 - 4]\rho^4. \tag{5.8}$$

Owing to the presence of γ_0 the first bifurcating branch in a domain with finite period may correspond to $n > 1$, where n is the number of wavelengths in the domain. The number of secondary branches is determined by the coefficient of ρ^4 in (5.8), and is finite when $(\gamma_1+a_1)^2 + 2b_1 < 4 + a_2^2$, a condition that is always satisfied in the case considered.

We compare here the predictions from the above equations, computed as in § 4, with the bifurcation behaviour seen in the original problem. To distinguish the different branches we have found it useful to plot the average three-dimensional kinetic energy, $\mathscr{E}' \equiv (1/2\Gamma)\int_D |\boldsymbol{u}|^2 \,\mathrm{d}x\,\mathrm{d}z$ as a function of Ra instead of $\mathscr{E}$, since in the latter representation all branches fall essentially on top of one another. Here

$$\mathscr{E}' = \tfrac{1}{2}\langle v_0^2\rangle + \tfrac{3}{8}\epsilon^2 k^2 \langle |a|^2\rangle + O(\epsilon^4), \tag{5.9}$$

where a is again defined as in (4.3). The bifurcation diagrams that result are shown in figure 18 for $\sigma = 0.6$, $\Gamma = 50\lambda_c$ and several different Taylor numbers near $T_+^{mod} \approx 5.1176$. The figure shows that there are two types of secondary branch and that both are strongly supercritical. Those represented in grey (red online) correspond to the convecton states studied in the full problem: the secondary bifurcations producing these states move towards small amplitude as the domain period Γ' increases, in agreement with the theory presented in § 4. However, as shown in figure 18(*a*), there is a second type of secondary state as well, represented by a dashed line. The presence of these states is a finite size effect: the secondary bifurcations producing these states move towards larger amplitude as Γ' increases. We refer to the latter as $n = 1$ defect states by analogy with other problems of this type (Bergeon *et al.* 2008); we have not

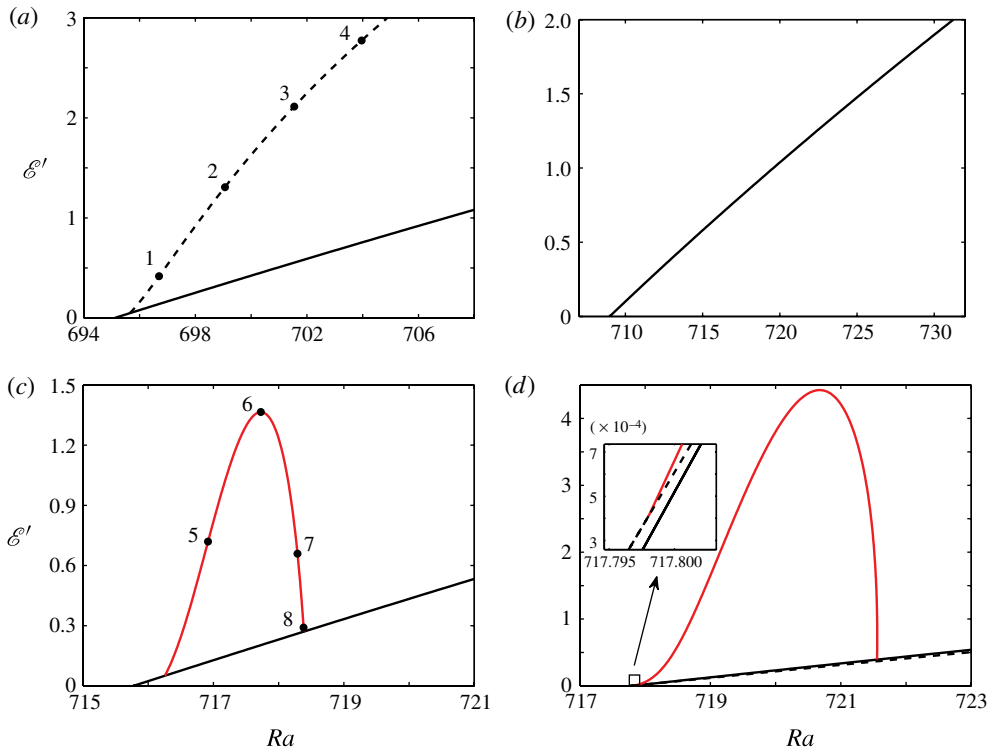

FIGURE 18. (Colour online) Bifurcation diagrams showing the average kinetic energy $\mathscr{E}'$ of the solutions of (5.3) satisfying NBC as a function of Ra for $\sigma = 0.6$ ($T_+^{mod} = 5.1176$), $T \sim T_+^{mod}$ and $\Gamma = 50\lambda_c$. Solid black lines: $\phi_X = 0$ primary state (periodic convection). Grey curves (red online): convectons. Dashed curve in: (*a*) modulated states called defect states; and (*d*) $\phi_X = 2\pi/\Gamma$ primary state. (*a*) $T = 4.4176$. (*b*) $T = 5.2176$. (*c*) $T = 5.5676$. (*d*) $T = 5.6676$.

computed states of this type in the full problem. Secondary branches of $n = 2, 3\ldots$ defect states may appear with further decrease of T. However, figure 18(*b*) shows that no secondary branches of either type are present when T is close to but below T_+^{mod}, as expected from the analysis in § 4. When we increase the Taylor number above T_+^{mod}, an $n = 1$ secondary branch bifurcates from the primary $\phi_X = 0$ branch at small but non-zero amplitude and reconnects to it at a subsequent secondary bifurcation (grey (red online) line in figure 18*c*). This is the convecton branch. For larger Taylor numbers, the left end of the convecton branch moves down to smaller amplitude and undergoes a phase jump to a $\phi_X \neq 0$ primary branch (figure 18*d*) while the right end remains on the $\phi_X = 0$ primary branch and moves up to larger amplitude. Figure 19 shows sample profiles of the amplitude $|A|$ along both branch types. These results may be compared with figure 13. We emphasize that the termination of the convecton branches cannot be determined within the cubic amplitude equation (4.13); for this purpose the non-local equation (5.3) is required.

It remains to mention that for $T = T_-^{mod}$ and $0 < \sigma \lesssim 0.59796$ the coefficient of $|A|^4 A$ is positive and a fifth-order calculation cannot capture the complete details of the transition whereby convectons disappear as T increases.

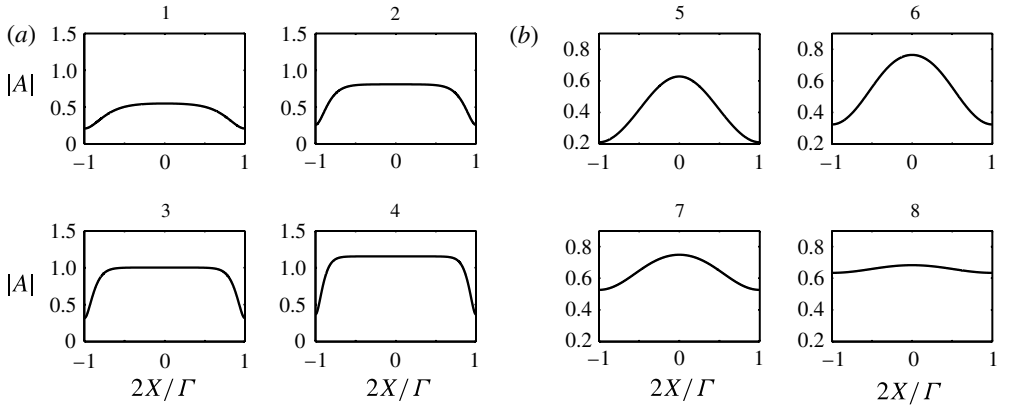

FIGURE 19. Sample solution profiles at the points 1–8 indicated in figure 18. (*a*) $T = 4.4176$. (*b*) $T = 5.5676$. Solutions in (*b*) correspond to convectons (grey curve in figure 18*c*), while those in (*a*) correspond to defect states (dashed curve in figure 18*a*).

6. Conclusion

In this paper we have computed strongly nonlinear solutions of the equations describing two-dimensional convection in a horizontal layer rotating with constant angular velocity about the vertical axis. The localized solutions were computed on spatially periodic domains with a period that is large compared to the critical wavelength of convection, and are present regardless of whether the primary branch of periodic states is sub- or supercritical, provided only that $\xi^2 > 1/3$. The localized structures are embedded in a self-generated zonal shear layer with a compensating shear profile outside the structure. The shear rate $V' < 0$ inside the convecton while $V' > 0$ outside, implying that the convecton locally reduces the angular velocity by expelling angular momentum; this angular momentum increases the angular velocity outside the convecton and creates a shear layer. Similar symbiotic coexistence between anticyclonic shear and localized vortex structures is familiar from other rotating fluid systems (Marshall & Schott 1999; Marcus, Kundu & Lee 2000; Evonuk & Glatzmaier 2007; Petersen, Julien & Stewart 2007).

In the present case the localized structures are present only for low Prandtl numbers ($\sigma < 1$) and moderate Taylor numbers. At small rotation rates the shear that accompanies a putative convecton is insufficient to localize it, while rotation rates that are too high suppress the amplitude of the convection and thereby the angular momentum expulsion that is required to confine the structure. However, when convectons are possible they are present over a substantial range of Rayleigh numbers (figure 10) in contrast to other fluid systems exhibiting localized states (Batiste *et al.* 2006; Lo Jacono *et al.* 2010; Beaume *et al.* 2011). This is a consequence of the conserved integral $\bar{V}$ of the zonal velocity $v(x, z, t)$ in the presence of stress-free boundary conditions at the top and bottom boundaries. Because of this conserved quantity the amplitude equations describing the localized structure are non-local, and the spatially periodic states are unstable at small amplitude even when they bifurcate supercritically. This non-local aspect of the problem has four consequences: (i) it leads to slanted snaking of the localized structures; (ii) it permits localized structures to

be present outside the region of bistability between the conduction state and periodic convection; (iii) it destabilizes the spatially periodic convection at small amplitude even when the bifurcation to convection is supercritical; and (iv) it permits localized states even when periodic convection bifurcates supercritically. These effects are all a consequence of the interaction between convection and the zonal shear flow it generates through the action of the Reynolds stresses associated with the convective flow. We have seen explicitly how the zonal shear flow generated by this mechanism can, under appropriate conditions, confine convection in the lateral direction thereby creating the localized structures studied in this paper.

The presence of slanted snaking permitted by the boundary conditions we use is significant since it greatly increases the Rayleigh number interval within which localized states may be found. The behaviour that results is similar to the slanted snaking present in convection in an imposed vertical magnetic field (Dawes 2007; Lo Jacono *et al.* 2011, 2012). As emphasized by Cox & Matthews (2001) this is a consequence of the conservation of imposed magnetic flux, a conserved quantity that exerts a qualitatively similar effect on the properties of localized states as exerted here by the requirement $\bar{V} = 0$. The effect of the conserved quantity persists as Γ increases (see e.g. figure 4). However, the limit $\Gamma \to \infty$ differs from the situation on the whole real line. In the latter case flux expulsion does not lead to an increase in the ambient magnetic field and the problem becomes *local*. This is the case for rotating convection as well: on the real line no prograde (anticyclonic) shear develops outside the convecton. It follows that with increasing Γ the slant of the snaking branches must decrease so that snaking in large domains ultimately becomes vertical. This is indeed the case when the *total* poloidal kinetic energy E is plotted as a function of Ra (Lo Jacono *et al.* 2011).

We emphasize that the wavelength within the convecton does not in general correspond to the wavelength of a coexisting periodic state, even if such a state is present. This is because the convecton wavelength is selected by the fronts on either side; because the convecton is spatially localized the wavelength within can vary with the applied Rayleigh number simply by adjusting the location of the fronts. This is not the case for periodic convection which is hemmed in by the imposed period Γ: for such states any increase in wavelength of one or more cells must be compensated by a corresponding wavelength decrease of the remaining cells. On the other hand centrifugal effects on a periodic cell state are usually neglected whenever $L\Omega^2/g \ll 1$, where $L \equiv \lambda$ is the dimensional wavelength. For convectons such as those described here the corresponding requirement is more stringent, since the relevant length scale L is now the convecton length, i.e. $L = N\lambda$, where N is the number of cell pairs within the structure.

In this work we have not studied the stability properties of the localized states we have calculated. These are complicated by the presence of Galilean invariance permitted by the stress-free boundaries we use, much as in non-rotating convection. In addition, in three dimensions these boundary conditions are responsible for the presence of a small-angle Küppers–Lortz instability (Clune & Knobloch 1993; Cox & Matthews 2000). Nevertheless, the third-order non-local amplitude equation studied in § 4 sheds light on the likely stability properties of the states we have found (Norbury *et al.* 2007), as does the fifth-order non-local equation derived in § 5, provided allowed perturbations are restricted to two dimensions.

Acknowledgements

This work was supported in part by Action Thématique de l'Université Paul Sabatier (CB) and the National Science Foundation under grants DMS-0908102 and DMS-1211953 (HCK & EK).

Supplementary data

Supplementary data are available at http://dx.doi.org/10.1017/jfm.2012.585.

Appendix. Direction of branching of the convecton branches

We begin with (4.8) and (4.9) and compute the secondary branch of stationary modulated solutions using weakly nonlinear theory, following Matthews & Cox (2000). These equations have the stationary equilibrium $(A, V) = (A_0, 0)$, where without loss of generality $A_0 = \sqrt{2r/(1-\xi^2)}$. We seek nearby solutions in the form

$$A = A_0(1 + \tilde{A}(X, \tau; \epsilon)), \quad V = \tilde{V}(X, \tau; \epsilon), \tag{A 1}$$

where $\tau = \epsilon^2 T_2$ and $\tilde{A} = \epsilon\tilde{A}_1 + \epsilon^2\tilde{A}_2 + \epsilon^3\tilde{A}_3 + \cdots$, $\tilde{V} = \epsilon\tilde{V}_1 + \epsilon^2\tilde{V}_2 + \epsilon^3\tilde{V}_3 + \cdots$. Here ϵ is defined implicitly by the relation $r = r_1 + \epsilon^2\tilde{r}$, where $r = r_1$ denotes the location of the secondary bifurcation. Since the imaginary part of $\tilde{A}$ decays to zero we take $\tilde{A}$ to be real. At $O(\epsilon)$ we obtain a linear eigenvalue problem for r_1 with solution $\tilde{A}_1 = \tilde{A}_{11}\cos lX$, $\tilde{V}_1 = \tilde{V}_{11}\sin lX$, where

$$r_1 = \frac{l^2}{2}\left(\frac{1-\xi^2}{3\xi^2-1}\right), \quad \tilde{V}_{11} = -\frac{4\xi r_1}{l(1-\xi^2)}\tilde{A}_{11}. \tag{A 2}$$

In the following we assume that $\xi^2 < 1$ so that the periodic state $(A_0, 0)$ is supercritical. Thus a secondary bifurcation requires that $3\xi^2 - 1 > 0$.

Second order

At $O(\epsilon^2)$ we obtain

$$\tilde{A}_{2XX} - 2r_1\tilde{A}_2 - \xi\tilde{V}_{2X} = 3r_1\tilde{A}_1^2 + \xi\tilde{A}_1\tilde{V}_{1X}, \tag{A 3}$$

$$\tilde{V}_{2X} + \frac{4\xi r_1}{1-\xi^2}\tilde{A}_2 = -\frac{2\xi r_1}{1-\xi^2}\tilde{A}_1^2 + C_2, \tag{A 4}$$

where C_2 is a constant of integration. The requirement that $\langle\tilde{V}_{2X}\rangle = 0$ determines C_2 and leads to the solution

$$\tilde{A}_2 = \tilde{A}_{20} + \tilde{A}_{22}\cos 2lX, \quad \tilde{V}_{2X} = \tilde{V}_{22}\cos 2lX, \tag{A 5}$$

where

$$\tilde{A}_{20} = \frac{7\xi^2-3}{4(1-\xi^2)}\tilde{A}_{11}^2, \quad \tilde{A}_{22} = \frac{1}{4}\tilde{A}_{11}^2, \quad \tilde{V}_{22} = -\frac{2\xi r_1}{1-\xi^2}\tilde{A}_{11}^2. \tag{A 6}$$

Third order

At $O(\epsilon^3)$ we obtain

$$\tilde{A}_{3XX} - 2r_1\tilde{A}_3 - \xi\tilde{V}_{3X} = 2\tilde{r}\tilde{A}_1 + 6r_1\tilde{A}_1\tilde{A}_2 + r_1\tilde{A}_1^3 + \xi\tilde{A}_2\tilde{V}_{1X} + \xi\tilde{A}_1\tilde{V}_{2X}, \tag{A 7}$$

$$\tilde{V}_{3X} + \frac{4\xi r_1}{1-\xi^2}\tilde{A}_3 = -\frac{4\xi\tilde{r}}{1-\xi^2}\tilde{A}_1 - \frac{4\xi r_1}{1-\xi^2}\tilde{A}_1\tilde{A}_2 + C_3. \tag{A 8}$$

The requirement $\langle \tilde{V}_{3X} \rangle = 0$ establishes that $C_3 = 0$. Elimination of terms proportional to $\cos lX$ from the equation for $\tilde{A}_3$ leads to the solvability condition

$$\tilde{r} = \frac{l^2}{4}\left(\frac{3 - 7\xi^2}{3\xi^2 - 1}\right)\tilde{A}_{11}^2, \tag{A 9}$$

where $l = 2\pi/\Gamma'$ and Γ' is defined in (4.26). It follows that the secondary branch is supercritical ($\tilde{r} > 0$) if $\xi^2 < 3/7$ and subcritical ($\tilde{r} < 0$) if $\xi^2 > 3/7$, in agreement with the numerical results in § 4. These results can also be obtained from a careful study of the conditions (4.21) using the potential $U[\rho]$ given in (4.20) with $K_1 = 0$ (Kao & Knobloch 2012).

We remark that Norbury *et al.* (2007) identify in their study of (4.8) and (4.9) only one type of secondary bifurcation, a supercritical one. In their work the bifurcation behaviour is described by the function

$$f(k) \equiv \frac{L^2}{8E(k)K(k)} + \frac{(1 - k^2/2)K(k)}{E(k)}, \tag{A 10}$$

where L is the domain length, and $E(k)$ and $K(k)$ are elliptic integrals of the first and second kind. Their result is based on the claim that $f(k)$ always attains a local minimum for some $k_0 \in (0, 1)$ owing to strict convexity ($f''(k) > 0$ for all $k \in (0, 1)$). However, an expansion of $f(k)$ around $k = 0$ shows that

$$f(k) = 1 + \frac{L^2}{2\pi^2} + \frac{k^4}{16}\left(1 - \frac{L^2}{4\pi^2}\right) + O(|k|^4). \tag{A 11}$$

Thus if $L < 2\pi$, f is non-decreasing and no local minimum is present. This in turn implies that the fold in the secondary branch is absent, i.e. that the secondary branch bifurcates subcritically. The condition $L = 2\pi$ agrees with that determined by Matthews & Cox (2000).

REFERENCES

ASSEMAT, P., BERGEON, A. & KNOBLOCH, E. 2008 Spatially localized states in Marangoni convection in binary mixtures. *Fluid Dyn. Res.* **40**, 852–876.

BAJAJ, K. M. S., AHLERS, G. & PESCH, W. 2002 Rayleigh–Bénard convection with rotation at small Prandtl numbers. *Phys. Rev.* E **65**, 056309.

BATISTE, O., KNOBLOCH, E., ALONSO, A. & MERCADER, I. 2006 Spatially localized binary-fluid convection. *J. Fluid Mech.* **560**, 149–156.

BEAUME, C., BERGEON, A. & KNOBLOCH, E. 2011 Homoclinic snaking of localized states in doubly diffusive convection. *Phys. Fluids* **23**, 094102.

BERGEON, A., BURKE, J., KNOBLOCH, E. & MERCADER, I. 2008 Eckhaus instability and homoclinic snaking. *Phys. Rev.* E **78**, 046201.

BERGEON, A. & KNOBLOCH, E. 2008 Spatially localized states in natural doubly diffusive convection. *Phys. Fluids* **20**, 034102.

BLANCHFLOWER, S. 1999 Magnetohydrodynamic convectons. *Phys. Lett.* A **261**, 74–81.

BURKE, J. & KNOBLOCH, E. 2007 Snakes and ladders: localized states in the Swift–Hohenberg equation. *Phys. Lett.* A **360**, 681–688.

CHANDRASEKHAR, S. 1961 *Hydrodynamic and Hydromagnetic Stability*. Oxford University Press.

CLUNE, T. & KNOBLOCH, E. 1993 Pattern selection in rotating convection with experimental boundary conditions. *Phys. Rev.* E **47**, 2536–2550.

COX, S. M. 2004 The envelope of a one-dimensional pattern in the presence of a conserved quantity. *Phys. Lett.* A **333**, 91–101.

COX, S. M. & MATTHEWS, P. C. 2000 Instability of rotating convection. *J. Fluid Mech.* **403**, 153–172.

COX, S. M. & MATTHEWS, P. C. 2001 New instabilities in two-dimensional rotating convection and magnetoconvection. *Physica* D **149**, 210–229.

DAWES, J. H. P. 2007 Localized convection cells in the presence of a vertical magnetic field. *J. Fluid Mech.* **570**, 385–406.

DAWES, J. H. P. 2008 Localized pattern formation with a large-scale mode: slanted snaking. *SIAM J. Appl. Dyn. Syst.* **7**, 186–206.

DAWES, J. H. P. & LILLEY, S. 2010 Localized states in a model of pattern formation in a vertically vibrated layer. *SIAM J. Appl. Dyn. Syst.* **9**, 238–260.

DOEDEL, E. J., CHAMPNEYS, A. R., DERCOLE, F., FAIRGRIEVE, T., KUZNETSOV, Y., OLDEMAN, B., PAFFENROTH, R., SANDSTEDE, B., WANG, X. & ZHANG, C. 2008*AUTO-07P: Continuation and Bifurcation Software for Ordinary Differential Equations*.

ECKHAUS, W. & IOOSS, G. 1989 Strong selection or rejection of spatially periodic patterns in degenerate bifurcations. *Physica* D **39**, 124–146.

ELMER, F. J. 1988 Nonlinear and non-local dynamics of spatially extended systems: stationary states, bifurcations and stability. *Physica* D **30**, 321–342.

ELMER, F. J. 1992 Parallels between pattern formation in high-power ferromagnetic resonance and fluid convection. In *Pattern Formation in Complex Dissipative Systems* (ed. S. Kai). pp. 309–313. World Scientific.

EVONUK, M. & GLATZMAIER, G. A. 2007 The effects of rotation rate on deep convection in giant planets with small solid cores. *Planet. Space Sci.* **55**, 407–412.

FIRTH, W. J., COLUMBO, L. & SCROGGIE, A. J. 2007 Proposed resolution of theory-experiment discrepancy in homoclinic snaking. *Phys. Rev. Lett.* **99**, 104503.

GOLDSTEIN, H. F., KNOBLOCH, E. & SILBER, M. 1990 Planform selection in rotating convection. *Phys. Fluids* A **2**, 625–627.

GOLDSTEIN, H. F., KNOBLOCH, E. & SILBER, M. 1992 Planform selection in rotating convection: hexagonal symmetry. *Phys. Rev.* A **46**, 4755–4761.

GUCKENHEIMER, J. & KNOBLOCH, E. 1983 Nonlinear convection in a rotating layer: amplitude expansions and normal forms. *Geophys. Astrophys. Fluid Dyn.* **23**, 247–272.

HALL, P. 1984 Evolution equations for Taylor vortices in the small-gap limit. *Phys. Rev.* A **29**, 2921–2923.

KAO, H.-C. & KNOBLOCH, E. 2012 Weakly subcritical stationary patterns: Eckhaus instability and homoclinic snaking. *Phys. Rev.* E **85**, 026211.

KNOBLOCH, E. 1998 Rotating convection: recent developments. *Intl J. Engng Sci.* **36**, 1421–1450.

LO JACONO, D., BERGEON, A. & KNOBLOCH, E. 2010 Spatially localized binary fluid convection in a porous medium. *Phys. Fluids* **22**, 073601.

LO JACONO, D., BERGEON, A. & KNOBLOCH, E. 2011 Magnetohydrodynamic convectons. *J. Fluid Mech.* **687**, 595–605.

LO JACONO, D., BERGEON, A. & KNOBLOCH, E. 2012 Spatially localized magnetoconvection. *Fluid Dyn. Res.* **44**, 031411.

MAMUN, C. K. & TUCKERMAN, L. S. 1995 Asymmetry and Hopf bifurcation in spherical Couette flow. *Phys. Fluids* **7**, 80–91.

MARCUS, P. S., KUNDU, T. & LEE, C. 2000 Vortex dynamics and zonal flows. *Phys. Plasmas* **7**, 1630–1640.

MARSHALL, J. & SCHOTT, F. 1999 Open-ocean convection: observations, theory, and models. *Rev. Geophys.* **37**, 1–64.

MATTHEWS, P. C. & COX, S. M. 2000 Pattern formation with a conservation law. *Nonlinearity* **13**, 1293–1320.

NORBURY, J., WEI, J. & WINTER, M. 2002 Existence and stability of singular patterns in a Ginzburg–Landau equation coupled with a mean field. *Nonlinearity* **15**, 2077–2096.

NORBURY, J., WEI, J. & WINTER, M. 2007 Stability of patterns with arbitrary period for a Ginzburg–Landau equation with a mean field. *Eur. J. Appl. Maths* **18**, 129–151.

PETERSEN, M. R., JULIEN, K. & STEWART, G. R. 2007 Baroclinic vorticity production in protoplanetary disks. I. Vortex formation. *Astrophys. J.* **658**, 1236–1251.

PROCTOR, M. R. E. 2001 Finite amplitude behaviour of the Matthews–Cox instability. *Phys. Lett.* A **292**, 181–187.

RIECKE, H. 1999 Localized structures in pattern-forming systems. In *Pattern Formation in Continuous and Coupled Systems* (ed. M. Golubitsky, D. Luss & S. H. Strogatz). pp. 215–229. Springer.

SCHNEIDER, T. M., GIBSON, J. F. & BURKE, J. 2010 Snakes and ladders: localized solutions of plane Couette flow. *Phys. Rev. Lett.* **104**, 104501.

SILBER, M. & KNOBLOCH, E. 1990 Travelling wave convection in a rotating layer. *Geophys. Astrophys. Fluid Dyn.* **51**, 195–209.

SILBER, M. & KNOBLOCH, E. 1993 Oscillatory convection in a rotating layer. *Physica* D **63**, 213–232.

VEGA, J. M. 2005 Instability of the steady states of some Ginzburg–Landau-like equations with real coefficients. *Nonlinearity* **18**, 1425–1441.

VERONIS, G. 1959 Cellular convection with finite amplitude in a rotating fluid. *J. Fluid Mech.* **5**, 401–435.

WEI, J. & WINTER, M. 2004 On a cubic-quintic Ginzburg–Landau equation with global coupling. *Proc. Am. Math. Soc.* **133**, 1787–1796.